Bending, Creasing, and Snapping of Soft, Slender Structures

Anupam Pandey

Thesis submitted to the Faculty of the
Virginia Polytechnic Institute and State University
in partial fulfillment of the requirements for the degree of

Master of Science
in
Engineering Mechanics

Douglas P. Holmes, Chair
Sunghwan Jung
James Hanna

July 21, 2014
Blacksburg, Virginia

Keywords: Bending, Creasing, Snapping, Beams, Shells

Bending, Creasing, and Snapping of Soft, Slender Structures

Anupam Pandey

(ABSTRACT)

Crosslinked polymers or elastomers are examples of soft, synthetic material that can bend, crease, snap, wrinkle in response to external stimulus like pH, humidity, electric field or swelling. If a droplet of favorable solvent is placed on top of a thin, elastomer beam, it bends drastically to accommodate the excessive swelling stress. Keeping the solvent and its volume constant if we just increase the thickness of the beam, microscopic surface creases appear on the top surface. In this thesis, we experimentally characterize this transition between global bending to surface creasing. Closing of Venus flytrap leaves is a classic example of well known snap-through instability. A knowledge of the timescale of snapping is crucial in designing advanced functional materials. We perform the simplest experiment of poking an soft, elastomer arch at its apex till it snaps. Combining our experiments with analytical model we are able to predict the purely geometric nature of the snapping timescale. We also develop a simple scaling law that captures the dynamics of jumping toy poppers.

To Babai, Mamoni, Babli and Dadu...

Acknowledgments

First of all, I would like to thank my thesis advisor Dr. Douglas P. Holmes for his guidance over the last three years. More than a mentor, Doug has always been a friend and philosopher to me. His creative approach towards solving a problem has influenced me the most. I thank him for introducing me to this beautiful world of experiments and painstakingly guiding me through this work. I believe this is just the start of our long scientific collaboration.

I am also grateful to my thesis committee members, Dr. Sunghwan Jung and Dr. James Hanna. Numerous discussions with Dr. Jung about interaction between fluid and soft solid have crucially helped shaping up this research. I thank James for entertaining my questions on differential geometry, elastica, dynamics and what not. I always knew he is the one whom I can discuss my queries with on any aspect of mechanics and even on a Friday evening.

I want to thank all the group members of Soft Mechanical Structures lab, particularly Behrouz Tavakol, Callan Gillespie and Trey Moore, for providing such a wonderful environment to work in. I would like to thank all my friends Wrik Mallik, Saikat Basu, Suvojit Ghosh, Surya Deb, Saikat Jana, Souvic Chatterjee, Abhijit Sarkar, Bikramjit Mukherjee, Brato Chakrabarti for all the fun and making my stay in Blacksburg a memorable one.

Most importantly, I thank my parents Haradhan Pandey (Babai) and Mitali Pandey (Mamoni), my sister Anamika Pandey (Babli), my late grandfather Bholanath Pandey (Dadu) for their endless love and support. My dad is the most influential person in my life. None of my academic pursuits would have been possible without him standing by my side. I thank my grandfather for realizing the importance of education in one's life and encouraging me to excel in it even though he had no formal education. Lastly, I must thank my wife Kaniska for being there for me all the time, for making me laugh when I was frustrated and for being a source of my inspiration.

Contents

List of Figures

List of Tables

Chapter 1

Introduction

Soft and slender structures are ubiquitous in natural and synthetic environments. The wrinkling of skin, snapping of Venus flytrap leaves, and the crumpling of soda cans are all examples of soft and thin structures deforming. The mechanics of thin objects is interesting because non-linear geometric effects give rise to beautiful shapes and fascinating patterns while the material properties remain linear. This makes soft, slender structures suitable for state of the art engineering applications such as flexible electronics, soft robotics and biomedical devices. This research is focused on understanding and controlling the shape of thin objects that undergo large deformations. We utilize osmotic swelling as a stimulus to generate surface creases, structural bending, and rapid snap buckling. Being able to predict and prescribe shape changes within soft materials will facilitate the rapid prototyping of adaptive structures, and allow dynamic instabilities to be used in advanced functional devices. This thesis aims to answer the following two questions: i. how does a polymeric structure respond to non-homogeneous swelling? and ii. how does geometry dictate the dynamic timescale of flexible snapping structures?

The most simple example of swelling induced deformation is the volumetric expansion of dry sponge when a water droplet is placed on it. The theory of poroelasticity is the dominant mathematical framework for describing the migration of fluid through a network, and it gives rise to a diffusion-like timescale known as poroelastic time, and is determined by the length and diffusivity of the material. The steady permeation of fluid through a porous network, and the equilibrium swelling of elastomers are well described by these diffusion dynamics, but the early time dynamics of soft, swelling polymers can be highly nontrivial. While most

of the available literature deals with wrinkling and creasing caused by homogeneous swelling of elastomers submersed in solvent, understanding the effect of elastomer geometry and fluid volume in the case of non-homogeneous swelling is still lacking. In the next chapter, We ask a very simple question, if a droplet of favorable solvent is placed on a dry elastomer, how does it accommodate the stress that develops? If a slender beam is exposed to a favorable solvent on one face, at long times it will reach a larger equilibrium length. At short times, the polymer chains in contact with the fluid elongate. This local expansion of elastic network creates a bilayer like structure in which the top layer wants to elongate in length, and thus it bends. Keeping the fluid volume constant, if we make the beam very thick, the flexural rigidity of the beam becomes larger than the moment induced by swelling, and the rigid structure imposes a compressive stress on the surface analogous to a surface confined elastomer, resulting the outermost layer of the structure to crease. We probed this transition between global bending to surface creasing experimentally, and developed a simple scaling that incorporates the fluid volume, its affinity to swell the polymer network and the beam thickness.

In chapter 3, we study the dynamics of snap-buckling instability. Even though the topic of snap-buckling is more than half a century old, the idea of harnessing the fast movement associated with this instability to generate functionality is fairly new. Use of elastomers that show large shape change without deforming plastically is crucial in designing such advanced, functional materials. Here we perform the simplest snap-through experiment of poking a thin, polymeric arch at its apex by a point load. Experiments show that the arch takes different energetically favorable configurations before losing contact with the indenter and snaps to an everted stable state. It vibrates like a under damped oscillator about the everted state before coming to rest. Combining our experiments with theoretical model we predict that the deformation mode, instability growthrate and after-snap ringing are all purely geometric in nature. We also show that the after-snap ringing is the source of the 'pop' sound that characterizes many snapping structures like toy poppers and jumping bimetallic disks.

Chapter 2

Swelling-Induced Deformations: A Materials-Defined Transition from Macroscale to Microscale Deformations

This work has been published in *Soft Matter*. Here it is reproduced by permission of The Royal Society of Chemistry.

2.1 Abstract

Swelling-induced deformations are common in many biological and industrial environments, and the shapes and patterns that emerge can vary across many length scales. Here we present an experimental study of a transition between macroscopic structural bending and microscopic surface creasing in elastomeric beams swollen non-homogeneously with favorable solvents. We show that this transition is dictated by the materials and geometry of the system, and we develop a simple scaling model based on competition between bending and swelling energies that predicts if a given solvent droplet would deform a polymeric structure macroscopically or microscopically. We demonstrate how proper tuning of materials and geometry can generate instabilities at multiple length scales in a single structure.

2.2 Introduction

Designing advanced materials to accommodate fluid-structure environments requires accurate control over the swelling-induced deformations of soft mechanical structures. The dynamics of osmotically driven movements within elastic networks, and the interplay between a structure's geometry and boundary conditions, play a crucial role in the morphology of growing tissues and tumors, [1, 2] the shrinkage of mud [3] and moss, [4] and the curling of cartilage, [5] leaves, [6, 7, 8] and pine cones. [9] Various structural and surface instabilities can occur when a favorable solvent is introduced to a dry gel. These include buckling, [10, 11, 12] creasing, [13] and wrinkling instabilities, [14, 15, 16, 17, 18, 19] and the curling of paper and rubber. [20, 21, 22, 23] In addition, porous thin films, such as fuel cell membranes, [24, 25] are highly susceptible to swelling-induced delamination and buckling, which cripple their functionality. For materials to adequately accommodate different fluid-structure environments there must be an accurate understanding of both the global and surface-confined deformations that can occur. In this paper, we examine the transition between global structural deformations and surface patterns that occur as a function of material geometry, fluid-structure interaction, and the volume fraction of the swelling fluid.

Building on the idea that soil can be treated as a porous elastic network, [26] the consolidation of fluid-saturated soil was examined, [27] and the mathematical framework for poroelasticity that emerged [28, 29, 30] remains the dominant theory for describing the migration of fluid within gels, [31, 32] tissues, [33, 34] and granular media. [35, 30] The fluid movement is dictated by the characteristic, or poroelastic, time required for it to move through a network. If the fluid and network are incompressible, and the fluid velocity obeys Darcy's law, [27] a diffusive-like time scale emerges: $\tau \sim L^2 D^{-1}$, where L is the characteristic length scale, and D is the diffusivity. The steady permeation of fluid through rigid porous networks, and the equilibrium swelling of crosslinked elastic networks are well described by these diffusion dynamics, but at early times the dynamic deformations of these soft, swelling elastomers can be highly nontrivial.

Material geometry, structural confinement, and non-homogenous exposure to fluid will all add additional complications to the swelling-induced deformations of soft mechanical structures. For instance, when the surface of a dry gel is exposed to favorable solvent, how does it accommodate the stress that develops? If a slender beam is exposed on one face to a favorable solvent the fluid will fully swell the beam at long times, and it will reach a larger

equilibrium length. [31, 36] At short times, the outer surface of the beam is under more stress than the bulk, and will elongate and bend into an arch. [23, 22, 21, 37, 38] However, bending of the structure will only occur if the swelling stress is greater than the stress required to bend the beam.

If the material is very thick, the resistance to bending will generate a compressive stress on the surface, causing the outermost layer of the structure to buckle. Biot was first to predict the presence of surface instabilities on a homogeneous elastic medium due to compressive forces. [39] Predicting and controlling these surface instabilities will impact the design of flexible electronics, soft robotics, and microfluidic devices. While most of the available literature on wrinkling and creasing deals with homogeneous swelling of confined gels submersed in solvent [14, 13, 40, 41] or soft substrates with stiff skins, [15, 16, 17, 19] understanding of the effect of elastomer geometry and fluid volume in case of the non-homogeneous swelling of gels is still lacking. We present a simple model experiment for probing this transition.

2.3 Materials and methods

Fig. 2.1 illustrates the experimental procedure. We place a favorable fluid droplet of volume V_f on top surface of an elastomeric beam having undeformed length L. As the fluid swells the polymeric network, we measured the length of the beam, $l(t)$, and surface topography, $\lambda(t)$, as a function of time. The schematic in figure 2.1a. shows the propagation of fluid within the crosslinked elastomer. The unswollen polymer coils within the network have an equilibrium radius of gyration, which will increase, *i.e.* swell, when the coil comes in contact with a solvent that has favorable enthalpic interactions (Fig. 2.1a - i. & ii.). A balance of the enthalpic interactions between the polymer and solvent and the entropic cost of stretching the chain dictate the extent of swelling within a given material system [42]. This local expansion of the elastic network creates a structure analogous to a bilayer, in which the top layer wants to be longer than the bottom layer, and thus it bends (Fig. 2.1b). If the flexural rigidity of the beam is larger than the moment induced by swelling, then the rigid structure will impose a compressive stress on the swollen layer, analogous to a gel that is constrained at its base (Fig. 2.1c). If this stress creates a compressive strain that exceeds a critical value, the surface will crease.

To study this transition between bending and creasing experimentally, we prepared poly-

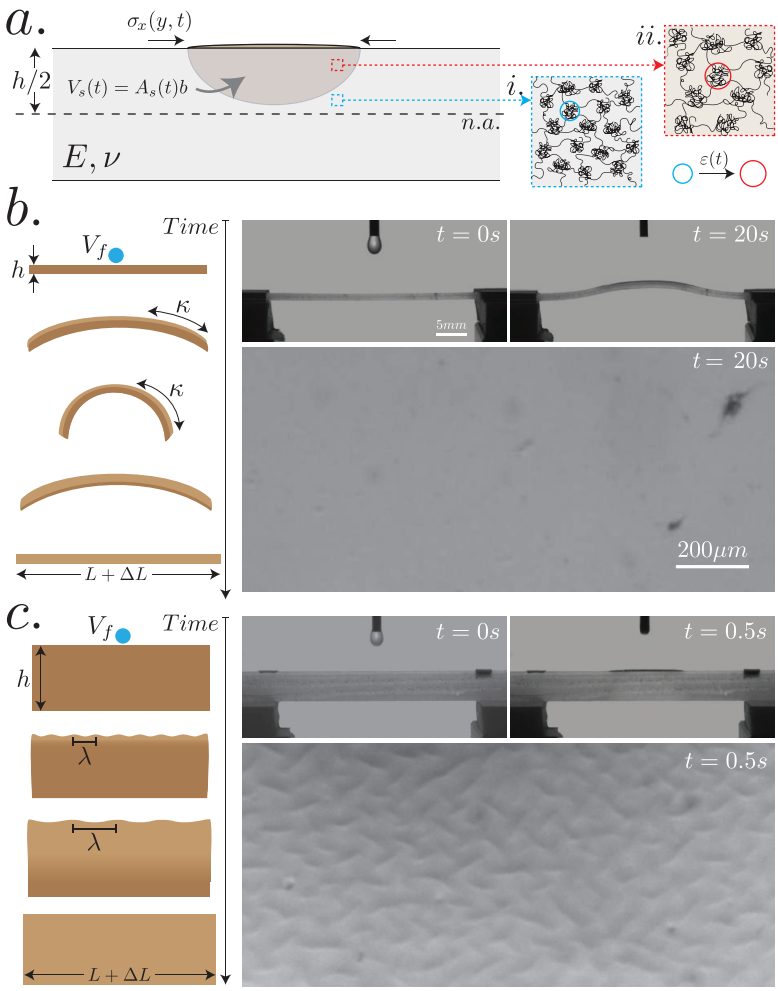

Figure 2.1: Bending and creasing of beams swollen non-homogenously. a.) A schematic showing the propagation of fluid through crosslinked polymer network. b.) A thin beam ($h = 1mm$, $L = 35mm$) is swollen by placing a diisopropylamine droplet of volume $5.96\mu L$ on its top surface. As the beam is fixed at both ends, it bends out of plane to accommodate the expansion of the top surface. c.) A much thicker beam ($h = 5mm$, $L = 35mm$) is swollen with the same solvent and volume, but instead of bending, creases appear on the top surface.

Table 2.1: Material solubility δ_s and polarity μ obtained from Lee *et al.*, [43] strain at equilibrium measured experimentally.

Material	δ_s $(cal^{1/2}cm^{-3/2})$	μ (D)	ε_{eq}
PDMS	7.3	0.6-0.9	–
Diisopropylamine	7.3	1.2	**1.13**
Triethylamine	7.5	0.7	**0.58**
Hexanes	7.3	0.0	**0.35**
Toluene	8.9	0.4	**0.31**
Ethyl acetate	9.0	1.8	**0.18**

dimethylsiloxane (PDMS) (Dow Corning Sylgard 184^{TM}) beams of various thicknesses (1 mm, 2 mm, 3 mm, 4 mm, 5 mm) with a width $b = 2.5\ mm$ and length $L = 35\ mm$ at a 10:1(w/w) ratio of prepolymer-to-crosslinker. A droplet of fluid was deposited at the middle of the beam by a syringe pump (New Era Pump Systems Inc, Model NE-1000), and its volume was varied from 1.29 μL to 5.96 μL by appropriate choice of syringe needle diameter (Hamilton). As the beam swells, its structural deformation was captured at 30fps using Edmund-Optics GigE camera with a Nikkor lens (35mm f: 1-1.4), while its surface deformation were recorded at 21 fps with a Edmund-Optics GigE camera attached with an inverted Nikkor lens (35mm f: 1-1.4) and a macro extension tube (Vivitar N-AF 36mm). Image analysis was performed using ImageJ and Matlab to extract the macroscopic beam elongation and microscopic crease wavelength as a function of time. Fluids were chosen based on their affinity for swelling PDMS, [43] which is comprised by similarities in both solubility δ_s and polarity μ (Table 2.1).

2.4 Results and discussion

The solubility and polarity of a fluid within a network combine in a nontrivial way to swell the elastic structure, [43] therefore the measured strain at equilibrium for a beam that is fully submersed in the fluid, ε_{eq}, is the metric we use to differentiate swelling ability. Fig. 2.2a shows the swelling of PDMS beams by five different fluids. Each beam is fully submerged in a solvent and its elongation is measured as a function of time. In this figure, we highlight the elongation at short times (*i.e.* $t \leq 100s$) to show that the beam initially deforms faster than the diffusive dynamics that drive swelling at long times, [44] and that the rate of this

early deformation differs for various solvents. In particular, we note that polarity differences between solvent and network may play an important role in the early time dynamics, with large deformations occurring when $|\Delta\mu| = |\Delta\mu_s - \Delta\mu_P| < 0.5$.

To study the transition between macroscopic structural deformation and surface deformation, we performed experiments with a finite volume of fluid. When a droplet of volume V_f is placed on the surface of a dry beam, a non-homogeneous strain field develops during swelling which propagates over time. For thin beams, a macroscopic strain is measured from the change in beam length, $\varepsilon = \frac{l-L}{L}$. Fig. 2.2b - i. shows a graph of ε as a function of time for two beams with different thicknesses that are exposed to 5.96 μL of diisopropylamine. We can quantify the maximum macroscopic strain ε_{max} that is achieved as a function of beam thickness (Fig. 2.2b - ii.) and fluid volume (Fig. 2.2b - iii.). Above a critical thickness, a particular type and volume of fluid is unable to generate enough stress to create a macroscopic deformation of the beam.We seek a reduced-order scaling analysis that will describe the material and geometric contributions to this critical threshold.

In these swelling-induced deformations, there exists an competition between the solvent's ability to swell the network, and the structure's ability to resist deformation. Since the swelling is non-homogenous, the strain variation through the thickness of the beam may induce a bending deformation. The rigidity of a structure can be quantified by the energy required to bend it, which is:

$$U_b = \int_0^L \frac{B}{2}(\theta'(s))^2 \mathrm{d}s \sim \frac{Ebh^3}{12(1-\nu^2)}, \tag{2.1}$$

where $B = \frac{Ebh^3}{12(1-\nu^2)}$, h is the thickness of the beam, b is the width of the beam, E is the elastic modulus, ν is Poisson's ratio, and $\theta(s)$ is the angle along the arc-length. Since the timescale of swelling is short, and the ratio of the fluid to the solid elastic network is very small, we assume a linear elastic behavior. If instead we allowed the swollen structures to approach chemical equilibrium, it would be necessary to consider a hyperelastic model where the elastic constants depend on the swelling strain. With these assumptions, we expect an energy due to swelling will take a similar form, with $U_s = \int_0^L \beta$, where β is a function of the elastic properties of the network, the interaction between the polymer and solvent, and the amount of fluid, *i.e.* $\beta = f(E, \varepsilon, V_f)$. If this takes the form of a strain energy, we may write $U_s \sim \int_{V_s} \sigma\ \epsilon\ \mathrm{d}V_s$, where V_s is the volume of the swollen region in the structure. With a finite volume of fluid, the maximum deformation will occur at short times during the

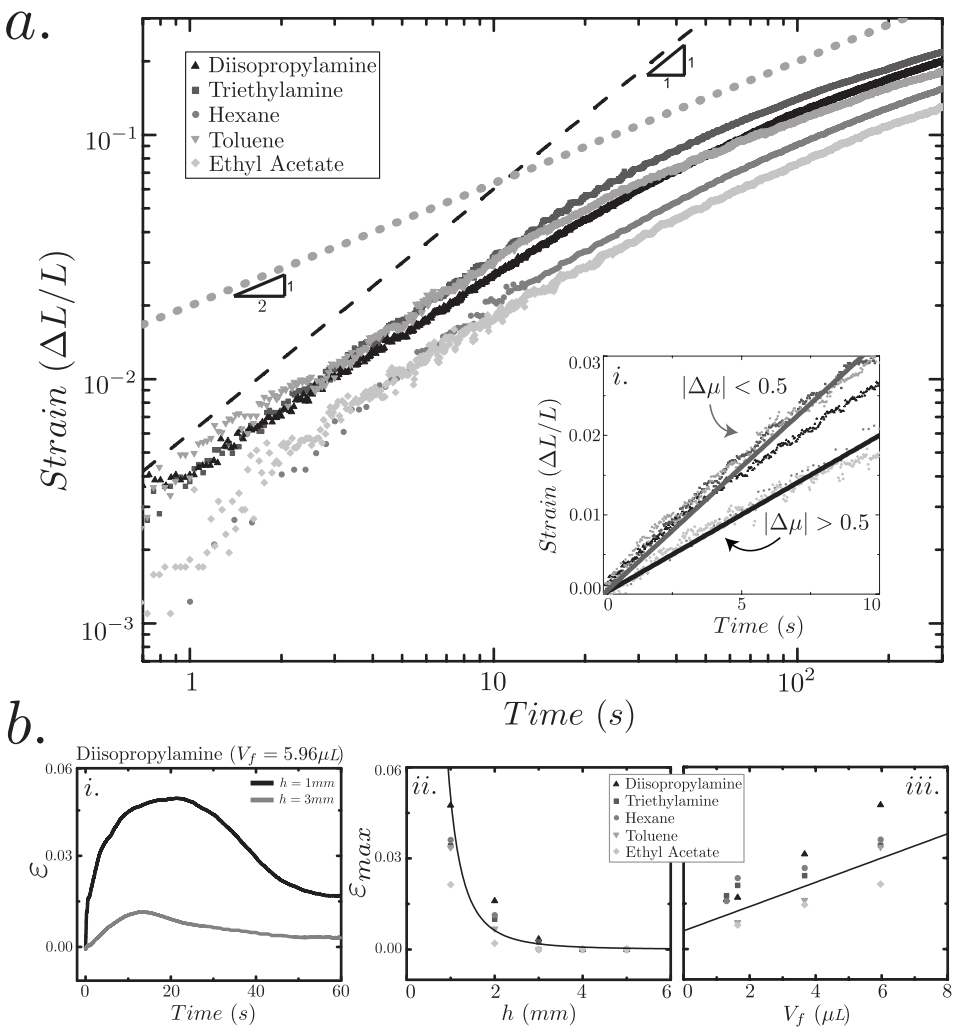

Figure 2.2: Swelling dynamics of PDMS at short times. a.) Submerged swelling strain of PDMS beams by different solvents. Inset: Different strain rates imparted by different solvents at short times. b.) i. Change in macroscopic strain($\varepsilon = \frac{l-L}{L}$) over a period of time when a Diisopropylamine droplet of volume $V_f = 5.96\mu L$ is placed on beams of thicknesses $1mm$, $3mm$. ii. Maximum strain(maximum ordinate in i.) developed in beams of various thicknesses due to $5.96\mu L$ droplet of all solvents. iii. Maximum strain in $1mm$ thick beam due to different droplet volume of all solvents.

swelling process, when there is a high concentration of solvent within a local region of the polymer network. If this small, but highly concentrated region is analogous to a fully swollen structure, then at short times we may assume that the strain imparted on these chains is on the order of the equilibrium swelling strain $\varepsilon \approx \varepsilon_{eq}$, and the volume of the swollen region will be confined to the volume of the fluid $V_s \approx V_f$. With these assumptions[1], we expect the swelling energy to scale as:

$$U_s = \int_{V_f} \sigma \; \varepsilon_{eq} \; \mathrm{d}V_f \sim Eb \; \varepsilon_{eq}^2 \; V_f. \tag{2.2}$$

The swelling-induced deformation of these beams will be dictated by the interplay between the bending and swelling energies, such that no bending will occur when $U_b >> U_s$. Hence these competition between bending and swelling energy gives rise to a length which we call *elastoswelling* length scale, ℓ_{es}:

$$\ell_{es} \sim \left(\varepsilon_{eq}^2 \; V_f\right)^{1/3}. \tag{2.3}$$

In the case of a transversely swollen beam, this length scale denotes a critical thickness below which bending will occur.

In figure 2.3a, we plot the experimentally observed maximum strain ε_{max} as a function of beam thickness normalized by this *elastoswelling* length, h/ℓ_{es}. The critical threshold determined from the reduced-order scaling prediction describes the onset of macroscopic bending very well. We observed macroscopic deformation with beams swollen by hexane and ethyl acetate slightly above $h/\ell_{es} = 1$, which may be attributed to an importance of $|\Delta\mu|$ at short times. Further experimental studies that focus on the impact of solvent-polymer polarity will be necessary to properly account for this phenomenon.

When $h > \ell_{es}$, the swelling-induced stress will be insufficient to macroscopically bend the structure, and the local expansion of the top surface of the beam will be restricted by the bulk PDMS network. Similar to gels that are confined to a rigid substrate, the restriction against bending will impart a compressive stress on the swelling region. If this compressive stress imparts a strain greater than $\epsilon = 0.35$, a locallized surface creasing instability will occur [39, 45, 46]. Fig. 2.3b shows the development of surface creases as a thick beam ($h = 5\ mm$) swells with diisopropylamine ($V_f = 5.96\ \mu L$) such that $h/\ell_{es} \approx 1.22$. Randomly

[1]Note: The assumption that $\varepsilon \approx \varepsilon_{eq}$ likely overestimates the local, short time strains within the polymer coils, while assuming that $V_s \approx V_f$ likely underestimates the volume of the swollen region at the time of maximum deformation.

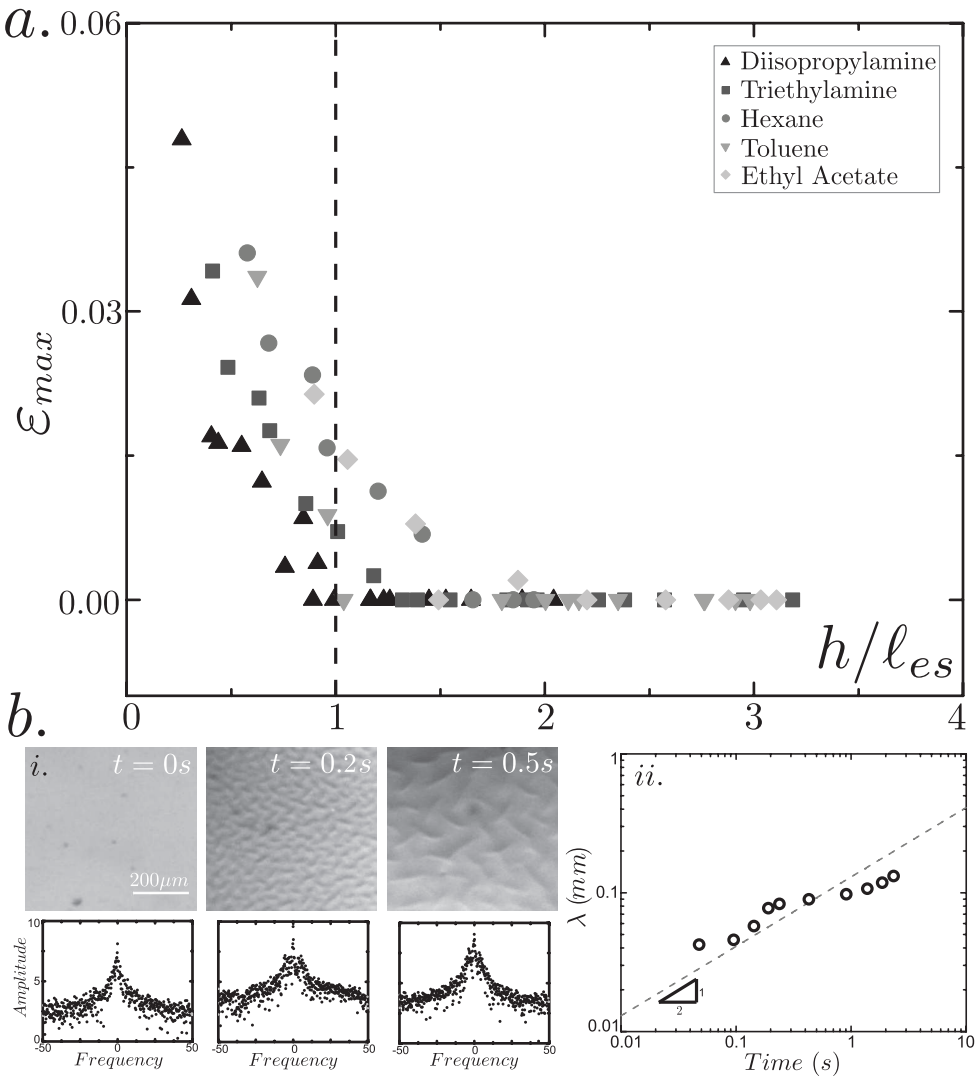

Figure 2.3: Transition between global bending to surface creasing. a.) Maximum strain in beams due to non-homogeneous swelling of different fluid droplet of different volume, as a function of beam thickness normalized by *elastoswelling* length. b.) Images of creases and their respective 2D FFT results. c.) Growth of crease spacing with time.

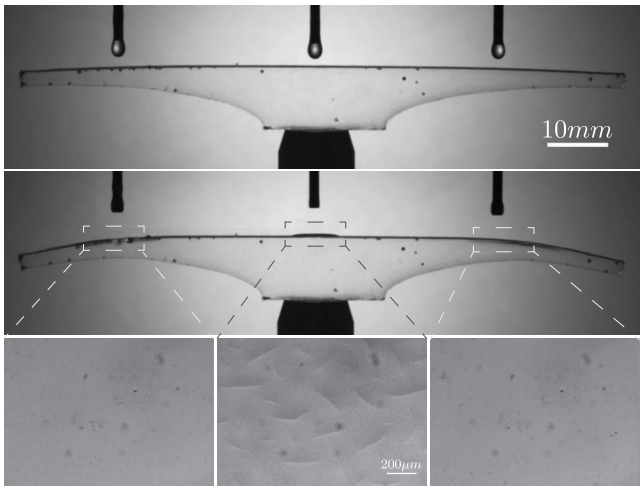

Figure 2.4: Bending and buckling. A structure with a variable thickness, such that it exhibits both bending in the thin regions and creasing in the thick regions for the same droplet size of solvent.

oriented surface-confined deformations appear immediately after swelling begins. Following the procedure described by Ebata *et al.*, [47] we performed a 2D Fast Fourier Transform (FFT) on the images to get the frequency and wavelength of these microstructures (Fig. 2.3b-i). At time zero, when no fluid is present, no structure is observed. On applying the fluid droplet, creases start to form across the surface, and peaks are evident on the amplitude vs. frequency plot. These peaks come closer to each other as the creases grow in length with time. Fig. 2.3b-ii. confirms the expected relation from Tanaka *et al.* [48] that the characteristic crease spacing will scale as $\lambda \sim t^{1/2}$. Our experimental results suggest that macroscopic deformation (bending) will occur when the thickness is below the *elastoswelling* length scale, *i.e.* $h/\ell_{es} < 1$, while microscopic deformations (creases) will form when $h/\ell_{es} > 1$. In the region where $h/\ell_{es} \approx 1$, a coexistence between both macroscale and microscopic deformations exist, suggesting that although we were unable to observe creases when $h/\ell_{es} < 1$, they may exist at very short times. Similarly, there will likely be an upper limit of h/ℓ_{es}, dictated by the surface strain, in which no deformation occurs. Our experimental approach makes accurately quantifying the local surface strains difficult, so determining this upper threshold is beyond the scope of this paper.

Finally, we demonstrate that both macroscopic structural and microscopic surface deformation can be generated in the same material by appropriately tuning the thickness. Fig. 2.4 shows a beam with a variable thickness along its length. In the thin regions, macroscopic

bending is observed and the surface remains smooth, while in the thick region the surface develops creases as it remains undeformed in macroscale. This represents a potential mechanism for controlling shape change and actuation across multiple length scales by generating deformation simultaneously on the microscale and the macro scale.

In summary, we have demonstrated a materials and geometry defined transition between a swelling-induced structural deformation and surface deformation. We present a scaling model that defines a critical *elastoswelling* length scale based on a balance of fluid-structure interactions, fluid volume, and the bending energy of the structure. Further experimental analyses are necessary to confirm the extension of this scaling to other geometries. Additionally, while our reduced-order model accurately captures the swelling-induced deformations in this paper, a more thorough theoretical model is required to quantitatively describe the scaling presented here. We anticipate that a better understanding of the nature of swelling-induced deformations of homogeneous materials will aid in designing and controlling shape change across many structural geometries and length scales. In particular, we provide a simple means for generating both the surface patterns and global shape within a structure using a given stimulus.

References

[1] B. Moulia. Leaves as shell structures: Double curvature, auto-stresses, and minimal mechanical energy constraints on leaf rolling in grasses. *Journal of Plant Growth Regulation*, 19(1):19–30, 2000.

[2] M. Ben Amar and A. Goriely. Growth and instability in elastic tissues. *Journal of the Mechanics and Physics of Solids*, 53(10):2284–2319, 2005.

[3] K A Shorlin, J R de Bruyn, M Graham, and St W Morris. Development and geometry of isotropic and directional shrinkage crack patterns. *Physical Review E*, 61(6):6950–6957, 2000.

[4] W Arnold. The cord moss and its allies . *Bryologist*, 2:52–55, 1899.

[5] L. A. Setton, H. Tohyama, and V. C. Mow. Swelling and curling behaviors of articular cartilage. *Journal of Biomechanical Engineering-Transactions of the ASME*, 120(3):355–361, 1998.

[6] M. J. King, J. F. V. Vincent, and W. Harris. Curling and folding of leaves of monocotyledons - A strategy for structural stiffness. *New Zealand Journal of Botany*, 34(3):411–416, 1996.

[7] S Nechaev and R Voituriez. On the plants leaves boundary, 'Jupe à Godets' and conformal embeddings. *J. Phys. A*, 34:11069–11082, 2001.

[8] M Marder, E Sharon, S Smith, and B Roman. Theory of edges of leaves. *Europhysics Letters (EPL)*, 62(4):498–504, May 2003.

[9] E. Reyssat and L. Mahadevan. Hygromorphs: from pine cones to biomimetic bilayers. *Journal of The Royal Society Interface*, 6(39):951–957, 2009.

[10] Y. Klein, E. Efrati, and E. Sharon. Shaping of Elastic Sheets by Prescription of Non-Euclidean Metrics. *Science*, 315(5815):1116–1120, 2007.

[11] D. P. Holmes and A. J. Crosby. Snapping Surfaces. *Advanced Materials*, 19(21):3589–3593, 2007.

[12] D. P. Holmes, M. Ursiny, and A. J. Crosby. Crumpled surface structures. *Soft Matter*, 4(1):82, 2008.

[13] Verónica Trujillo, Jungwook Kim, and Ryan C. Hayward. Creasing instability of surface-attached hydrogels. *Soft Matter*, 4(3):564, 2008.

[14] T. Tanaka, S-T. Sun, Y. Hirokawa, S. Katayama, J. Kucera, Y. Hirose, and T. Amiya. Mechanical Instability of Gels at the Phase-Transition. *Nature*, 325(6107):796–798, 1987.

[15] E P Chan and A. J. Crosby. Spontaneous formation of stable aligned wrinkling patterns. *Soft Matter*, 2(4):324, 2006.

[16] D Breid and A. J. Crosby. Surface wrinkling behavior of finite circular plates. *Soft Matter*, 5(2):425, 2009.

[17] Hyun Suk Kim and Alfred J Crosby. Solvent-responsive surface via wrinkling instability. *Advanced Materials*, 23(36):4188–92, September 2011.

[18] W Barros, E N de Azevedo, and M Engelsberg. Surface pattern formation in a swelling gel. *Soft Matter*, 8(32):8511, 2012.

[19] J Kim, J A Hanna, M Byun, C D Santangelo, and R C Hayward. Designing Responsive Buckled Surfaces by Halftone Gel Lithography. *Science*, 335(6073):1201–1205, March 2012.

[20] S. Douezan, M. Wyart, F. Brochard-Wyart, and D. Cuvelier. Curling instability induced by swelling. *Soft Matter*, 7(4):1506, 2011.

[21] C. Nah, G. B. Lee, C. I. Lim, J. H. Ahn, and A. N. Gent. Swelling of Rubber under Nonuniform Stresses and Internal Migration of Swelling Liquid When the Stresses Are Removed. *Macromolecules*, pages 1610–1614, February 2011.

[22] E Reyssat and L Mahadevan. How wet paper curls. *Europhysics Letters*, 93:54001, 2011.

[23] Douglas P. Holmes, Matthieu Roché, Tarun Sinha, and Howard A. Stone. Bending and twisting of soft materials by non-homogenous swelling. *Soft Matter*, 7(11):5188, 2011.

[24] Y Tang, A M Karlsson, M H Santare, M Gilbert, S Cleghorn, and W B Johnson. An experimental investigation of humidity and temperature effects on the mechanical properties of perfluorosulfonic acid membrane. *Materials Science and Engineering: A*, 425(1-2):297–304, 2006.

[25] Y Zhou, G Lin, A J Shih, and S J Hu. Assembly pressure and membrane swelling in PEM fuel cells. *Journal of Power Sources*, 192(2):544–551, 2009.

[26] K Terzaghi. Principle of Soil Mechanics. *Eng. News Record*, 1925.

[27] M A Biot. General Theory of three-dimensional consolidation. *Journal of Applied Physics*, 12:155–164, 1941.

[28] M J Crochet and P M Naghdi. On constitutive equations for flow of fluid through an elastic solid. *Int. J. Eng Sci.*, 4:383–401, 1966.

[29] L W Morland. A simple constitutive theory for a fluid-saturated porous solid. *Journal of Geophysical Research*, 77(5):1–11, 1972.

[30] H F Wang. *Theory of Linear Poroelasticity with Applications to Geomechanics and Hydrogeology*. Princeton University Press, Princeton, 2000.

[31] T. Tanaka and D. J. Fillmore. Kinetics of swelling of gels. *The Journal of Chemical Physics*, 70(03):1214–1218, 1979.

[32] J Dolbow, E Fried, and H Ji. Chemically induced swelling of hydrogels. *Journal of the Mechanics and Physics of Solids*, 52(1):51–84, 2004.

[33] J. M. Skotheim and L. Mahadevan. Physical Limits and Design Principles for Plant and Fungal Movements. *Science*, 308:1308–1310, 2005.

[34] S C Cowin and S B Doty. *Tissue Mechanics*. Springer, 2006.

[35] J Bear. *Dynamics of Fluids in Porous Media*. Dover, New York, 1988.

[36] Yong Li and Toyoichi Tanaka. Kinetics of swelling and shrinking of gels. *The Journal of Chemical Physics*, 92(2):1365, 1990.

[37] A. Lucantonio and P. Nardinocchi. Reduced models of swelling-induced bending of gel bars. *International Journal of Solids and Structures*, 49(11-12):1399–1405, June 2012.

[38] A. Lucantonio, P. Nardinocchi, and L. Teresi. Transient analysis of swelling-induced large deformations in polymer gels. *Journal of the Mechanics and Physics of Solids*, 61(1):205–218, January 2013.

[39] M A Biot. Surface instability of rubber in compression. *Appl Sci. Res., Sect. A*, 12:168–182, 1961.

[40] Samuel James DuPont Jr., Ryan Scott Cates, Peter George Stroot, and Ryan Toomey. Swelling-induced instabilities in microscale, surface-confined poly(N-isopropylacryamide) hydrogels. *Soft Matter*, 6(16):3876, 2010.

[41] Dayong Chen, Shengqiang Cai, Zhigang Suo, and Ryan Hayward. Surface Energy as a Barrier to Creasing of Elastomer Films: An Elastic Analogy to Classical Nucleation. *Physical Review Letters*, 109(3):1–5, July 2012.

[42] P.J. Flory. *Principles of Polymer Chemistry*. Cornell University Press, Ithaca, NY, 1953.

[43] Jessamine Ng Lee, Cheolmin Park, and George M Whitesides. Solvent compatibility of poly(dimethylsiloxane)-based microfluidic devices. *Analytical Chemistry*, 75(23):6544–54, December 2003.

[44] Masao Doi. Gel Dynamics. *Journal of the Physical Society of Japan*, 78(5):052001, April 2009.

[45] Shengqiang Cai, Dayong Chen, Zhigang Suo, and Ryan C. Hayward. Creasing instability of elastomer films. *Soft Matter*, 8(5):1301, 2012.

[46] Shengqiang Cai, Katia Bertoldi, Huiming Wang, and Zhigang Suo. Osmotic collapse of a void in an elastomer: breathing, buckling and creasing. *Soft Matter*, 6(22):5770, 2010.

[47] Yuri Ebata, Andrew B. Croll, and Alfred J. Crosby. Wrinkling and strain localizations in polymer thin films. *Soft Matter*, 8(35):9086, 2012.

[48] H Tanaka, H Tomita, a Takasu, T Hayashi, and T Nishi. Morphological and kinetic evolution of surface patterns in gels during the swelling process: Evidence of dynamic pattern ordering. *Physical Review Letters*, 68(18):2794–2797, May 1992.

Chapter 3

Dynamics of Snapping Beams and Jumping Poppers

This work has been done in collaboration with Derek E. Moulton and Dominic Vella at Mathematical Institute, University of Oxford. While we performed all the experiments, Derek E. Moulton and Dominic Vella developed the analytical model for this problem. For the original publication refer to : *EPL (Europhysics Letters)*. Here it is reproduced by permission of the Europhysics Letters Association (EPLA).

3.1 Abstract

We consider the dynamic snapping instability of elastic beams and shells. Using the Kirchhoff rod and Föppl-von Kármán plate equations, we study the stability, deformation modes, and snap-through dynamics of an elastic arch with clamped boundaries and subject to a concentrated load. For parameters typical of everyday and technological applications of snapping, we show that the stretchability of the arch plays a critical role in determining not only the post-buckling mode of deformation but also the timescale of snapping and the frequency of the arch's vibrations about its final equilibrium state. We show that the growth rate of the snap-through instability and its subsequent ringing frequency can both be interpreted physically as the result of a sound wave in the material propagating over a distance comparable to the length of the arch. Finally, we extend our analysis of the ringing frequency of indented arches to understand the 'pop' heard when everted shell structures

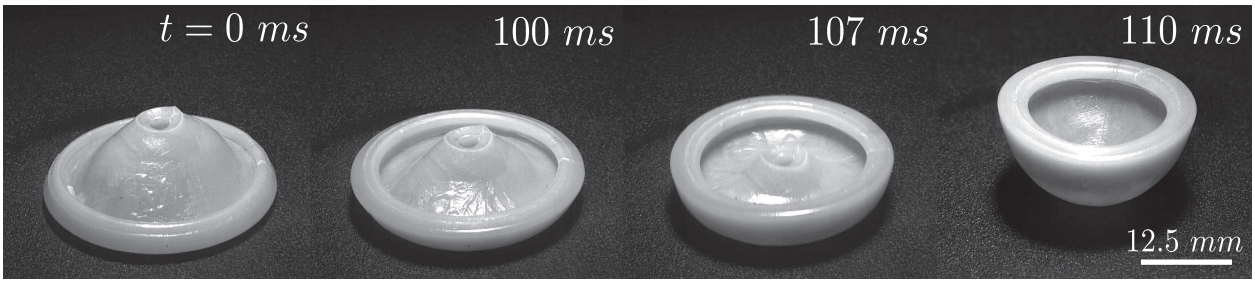

Figure 3.1: Snap-through of a commercially available child's popper ($E \approx 25\,MPa$ and $\rho \approx 1200\,kg/m^3$) from a flat surface.

snap-through to their stable state. Remarkably, we find that not only are the scaling laws for the ringing frequencies in these two scenarios identical but also the respective prefactors are numerically close; this allows us to develop a master curve for the frequency of ringing in snapping beams and shells.

3.2 Introduction

Arched structures have been used in architecture for over four thousand years [1], and the stability of these bistable structures has captivated scientists for over a century [2, 3]. The use of arches in engineering environments has traditionally placed a substantial focus on predicting the onset of stability loss, and the subsequent unstable modes of deformation [4, 5, 6, 7, 8, 9]. More recently, the potential utility of controlling structural stability loss to take advantage of the rapid transition between two stable shapes has been the focus of study. Not only can a large deformation be achieved quickly, but frequently with little energetic cost. Nature has long made use of such elastic instabilities for functionality, with the carnivorous waterwheel plant [10] and Venus flytrap [11, 12] using their elaborate snapping leaves to rapidly capture their prey. Meanwhile, snapping shells have captivated children for decades in the form of bimetallic "jumping" disks [13] and rubber toy "poppers" [14, 15] that, having first been turned 'inside-out' leap from a table with an audible pop as they return to their stable state (see fig. 3.1). These same principles have recently been used in the development of switches within MEMS devices [16, 17], biomedical valves [18], switchable optical devices [19], responsive hydrogels [20], and aerospace engineering [21, 22].

Traditionally, studies of snapping have focussed on the conditions under which a shell or

deformed beam can remain in equilibrium [23, 11]. Previous work on dynamic buckling tends to focus on how the critical load to induce snapping depends on the dynamics of loading [24, 25]. However, in the design of advanced materials an understanding of the dynamics of snapping itself is necessary to make full use of the snapping transition. In this Letter, we study the dynamics of snapping using a combination of experiments and theoretical calculations.

3.3 Experiments

Motivated by the 'snap-through' of a popper shown in Fig. 3.1, we first study the snapping dynamics of a much simpler system: a two-dimensional elastic arch subject to a point load. We consider a shallow arch loaded by a point at its apex, and demonstrate the importance of the beam's 'stretchability' on both the form of deformation and the snapping dynamics. In contrast to recent work that has focused on snapping induced by a fixed load [26, 25], we consider the limit of 'displacement control'.

Fig. 3.2a illustrates the setup considered here: a clamped beam of length L, thickness h, and width b is compressed by an axial displacement ΔL so that it buckles into an arch. An imposed displacement is then applied as a line load to the midpoint between the two clamped ends [1]. The initial height of the apex before indentation is w_0. Qualitatively speaking, we observe that for shallow arches, the beam remains symmetric about its center throughout the loading (fig. 3.2a.(I.)), while deep arches transition from a symmetric to an asymmetric shape well before snap-through occurs (fig. 3.2a.(i.)). In both cases, once the neutral axis of the beam is displaced to the mid-point of the clamped edges, global stability is lost, and the beam undergoes rapid snap-buckling to an inverted arch. To understand these observations, we begin by considering the motion before snapping, which we assume is quasi-static, before moving on to study the dynamics of snapping and ringing.

We model the shape of the deformed beam using both the Kirchhoff equations for elastic rods and the Föppl-von Kármán (FvK) equations [27]. In the following discussion, we shall present the results of the FvK theory since this more easily allows for the identification of the

[1] Polyvinylsiloxane (PVS, Elite 22, $Zhermack^{TM}$, $E = 789.49\ kPa$ beams were prepared with stretchability $\mathcal{S}_1 = 1.912 \times 10^{-4}$ and $\mathcal{S}_2 = 9.706 \times 10^{-4}$. The ends of the beam were clamped by embedding them within crosslinked polydimethylsiloxane (PDMS) (Dow corning Sylgard 184^{TM}). The indentation was performed in an Instron 5848 Microtester and the force was measured by Interface ULC 0.5 N load cell.

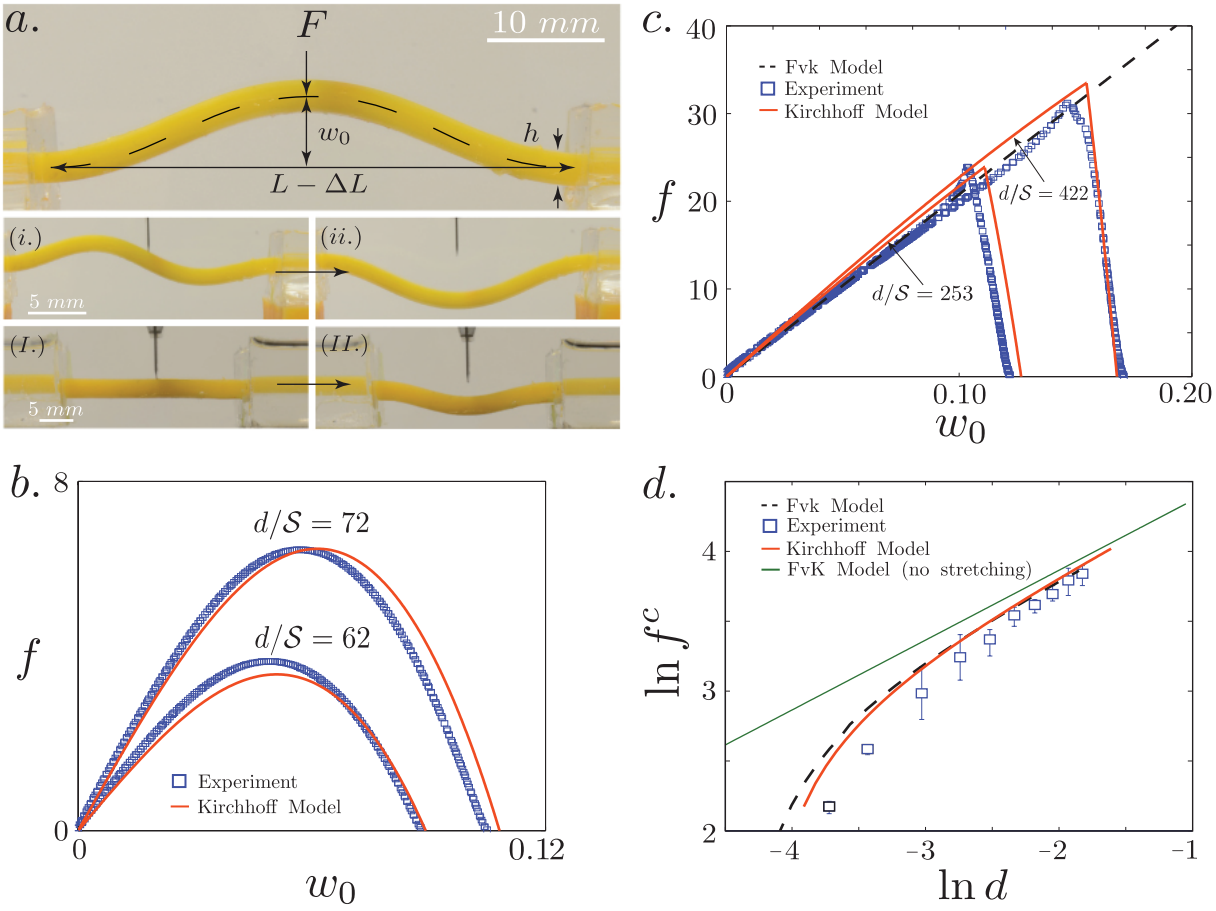

Figure 3.2: Snap-through of a two-dimensional arch loaded along a line. a.) Experimental set-up showing a Polyvinylsiloxane(PVS) arch with both ends clamped and loaded at its apex by a razor blade. (i) and (ii) show the asymmetric deformation mode of a deep arch and the subsequent snap-through to the inverted stable configuration. (I) and (II) show a shallow arch going through a flat mode of deformation and snapping. Force-displacement plots for arches that b.) remain symmetric throughout and c.) first deform symmetrically but then asymmetrically. d.) Maximum force f^c as a function of end–end compression d for stretchability $\mathcal{S}_1 = 1.912 \times 10^{-4}$.

important parameters and the calculation of asymptotic results. However, numerical results from the Kirchhoff theory are used in comparisons with experiment since these account correctly for the effect of large displacements.

3.4 FvK model

In the case of small transverse displacement, the profile of the arch is denoted by $w(x,t)$, which satisfies the dimensionless dynamic beam equation [27]

$$\frac{\partial^2 w}{\partial t^2} + \frac{\partial^4 w}{\partial x^4} + \tau^2 \frac{\partial^2 w}{\partial x^2} = f\delta(x), \quad -1/2 < x < 1/2. \tag{3.1}$$

Here, $\tau^2 = TL^2/B$ is the dimensionless compressive force (with T the dimensional axial load applied), B is the bending modulus $B = Eh^3b/12$ (with E the Young modulus), ρ_s is the density of the material and $f = FL^2/B$ is the dimensionless indentation force applied at the center of the beam. Time is non-dimensionalized by $t_* = L^2\sqrt{12\rho_s hb/Eh^3b} = 2\sqrt{3}L^2/ch$, with $c = \sqrt{E/\rho_s}$ the sound speed within the material.

The out-of-plane deflection w is coupled to the in-plane horizontal displacement u by Hooke's law relating the compressive stress to the higher-order von Kármán strain. In dimensionless terms, this reads

$$-\mathcal{S}\tau^2 = \frac{\partial u}{\partial x} + \frac{1}{2}\left(\frac{\partial w}{\partial x}\right)^2, \tag{3.2}$$

where

$$\mathcal{S} = \frac{B}{EhL^2b} = \frac{h^2}{12L^2}$$

is the 'stretchability' of the beam and is a measure of the relative importance of bending and stretching energies. The importance of stretchability has been discussed previously for vibrations about equilibrium within the Kirchhoff formalism [28] and in the context of wrinkling plates[29], though the analytical results and experiments presented here are, to our knowledge, new.

The clamped boundary conditions at the two ends of the arch are given by $w(\pm 1/2) = w'(\pm 1/2) = 0$ while the horizontal compression is imposed by the condition $u(\pm 1/2) = \mp d/2$, where $d = \Delta L/L$ is the dimensionless end-shortening.

3.5 Quasi-static evolution

To study the deformation prior to snapping we assume that loading occurs quasistatically and so consider time-independent solutions of (3.1), i.e. we neglect the $\partial_t^2 w$ term. It is possible to solve the quasi-static equation for the shape of the indented beam analytically, the unknown indentation force f being determined in terms of w_0 as part of the solution (for details, see appendix A.2).

Our analysis reveals that the form of deformation depends on the value of $d/\mathcal{S}$. First, if $d/\mathcal{S} < 4\pi^2$, the compressed, unbuckled beam is stable; neither buckling nor snapping occur as the in-plane compression does not induce Euler buckling in the beam. This can be understood in physical terms as follows: a compression ΔL corresponds to a strain d, a stress Ed or a compressive force $Ehbd$ on the beam. However, the buckling load for a beam with clamped edges is well-known to be $F = 4\pi^2 B/L^2 = 4\pi^2 \mathcal{S} Ehb$; hence when $d < 4\pi^2\mathcal{S}$ buckling cannot occur. In what follows the quantity $d - 4\pi^2\mathcal{S}$ frequently occurs and should be interpreted physically as the end-end compression that remains after some of the applied confinement of the beam has been accommodated by compressing the beam in response to the buckling load.

If $4\pi^2 < d/\mathcal{S} < \tau_{\max}^2 \approx 80.76$ (with $\tau_{\max} \approx 8.99$ the solution of $\tau_{\max}/2 = \tan(\tau_{\max}/2)$), the arch remains symmetrical as it deforms, ultimately returning to the compressed flat state $w = 0$ (at which point snapping is observed experimentally).

For $d/\mathcal{S} > \tau_{\max}^2 \approx 80.76$, an asymmetric mode appears, in addition to the symmetric mode, once the indentation reaches a critical value or, equivalently, a critical force. Detailed calculations (appendix A.2.3) show that this asymmetric mode is energetically favourable whenever it exists. In the asymmetric mode, the force-displacement relation is linear, $f = -207.75 w_0$, and the compressive force τ remains constant at $\tau = \tau_{\max} \approx 8.897$. The FvK analysis also shows that the critical indentation force is given by

$$f^{(c)} = -207.75 w_0^{(c)} = -129.53(d - 80.76\mathcal{S})^{1/2}. \tag{3.3}$$

While the theory could be tested by comparing theoretical and experimental beam shapes, a more rigorous test is to compare the force-displacement relationship predicted theoretically with that measured experimentally for each of the three regimes discussed above. In experiments, we have used beams with two different stretchabilities: $\mathcal{S}_1 = 1.912 \times 10^{-4}$ and

$\mathcal{S}_2 = 9.706 \times 10^{-4}$. The regime of buckled beams with small compression ($4\pi^2 < d/\mathcal{S} < \tau^2_{\max} \approx 80.76$) is somewhat difficult to explore experimentally since the weight of the beam becomes important in this case. Therefore, to explore the force-displacement relation for arches in this regime we use the beam with relatively high stretchability ($\mathcal{S}_2 = 9.706 \times 10^{-4}$); the force-displacement plot in this case is shown in fig. 3.2b. For the regime of large compression, $d/\mathcal{S} > \tau^2_{\max} \approx 80.76$, no such restriction applies; a comparison of theory and experiment in this regime, for two different values of $d/\mathcal{S}$, is shown in fig. 3.2c.

Note that finite stretchability plays a crucial role in the picture outlined above. First, if stretchability is neglected, $\mathcal{S} = 0$, then the family of beam shapes that return to a flat, compressed beam at $w_0 = 0$ (observed when $d < \tau^2_{\max}\mathcal{S}$) cannot occur. Second, even when $d/\mathcal{S} > \tau^2_{\max}$ the critical transition force between symmetric and asymmetric deformations predicted in (3.3) is sensitive to the amount of stretchability, as is also seen experimentally (Fig 3.2d). It is in only in the high arch regime that stretchability becomes negligible [26].

One final result from the study of the quasi-static indentation of an arch visible in fig. 3.2b,c is vital for our study of snapping: regardless of which deformation mode occurs, i.e. independently of the precise value of $d/\mathcal{S}$, the indentation force and w_0 vanish together. This is also similar to what is observed in the confinement of a buckled arch in a shrinking box [30, 31]. If $4\pi^2 < d/\mathcal{S} < \tau^2_{\max}$, the solution at this point is the flat compressed beam, while for $d/\mathcal{S} > \tau^2_{\max}$, the beam has the form of the antisymmetric, mode 2 Euler buckling. In both cases, if the indentation were to continue, symmetry dictates that the indentation force would have to become negative. In the absence of any adhesion between indentor and arch, this is not possible and so no equilibrium solution is possible — contact must be lost and the beam must then 'snap-through' to the stable state, the inverted arch. This explains the experimental observation that snap-through occurs when the neutral axis of the beam is displaced to the mid-point of the clamped edges.

3.6 Dynamics of snapping and ringing

To understand the timescale of snap-through, we perform a linear stability analysis of the beam at the point at which contact with the indentor is lost. We set $f = 0$ in eqn.(3.1) and look for solutions of the form $w(x,t) = w_\alpha(x) + \epsilon w_p(x) e^{\sigma t}$, where $w_\alpha(x)$ is the shape at the point of snapping ($\alpha = 0, 2$ depending on whether snapping occurs from the flat or

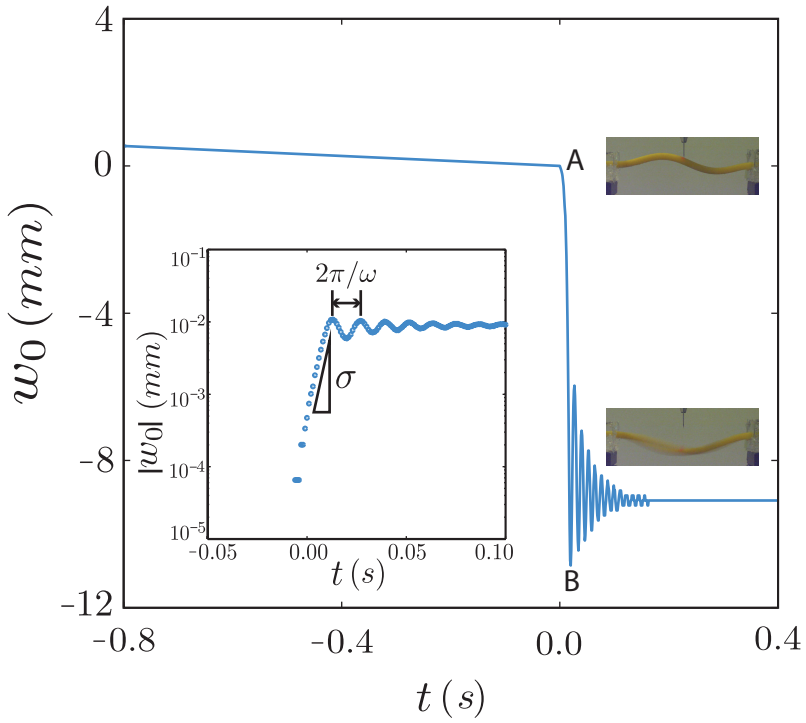

Figure 3.3: Dynamics of arch snap-through. Main figure: Experimentally measured displacement of the central point as the arch snaps and vibrates. Inset: Semilog plot of displacement vs. time, showing the growth rate σ and vibration frequency ω after, snapping.

asymmetric modes). We also perturb the compressive force, $\tau = \tau_\alpha + \epsilon\tau_p e^{\sigma t}$. At leading order in ϵ we obtain an eigenvalue problem for the growth rate σ with eigenfunction $w_p(x)$ satisfying

$$\frac{\mathrm{d}^4 w_p}{\mathrm{d}x^4} + \tau_\alpha^2 \frac{\mathrm{d}^2 w_p}{\mathrm{d}x^2} + \sigma^2 w_p = -2\tau_\alpha \tau_p \frac{\mathrm{d}^2 w_\alpha}{\mathrm{d}x^2}, \tag{3.4}$$

$$\int_{1/2}^{1/2} \frac{\mathrm{d}w_\alpha}{\mathrm{d}x}\frac{\mathrm{d}w_p}{\mathrm{d}x}\mathrm{d}x = -2\mathcal{S}\tau_\alpha\tau_p, \tag{3.5}$$

along with boundary conditions $w_p(\pm 1/2) = w_p'(\pm 1/2) = 0$. The eigenproblem (3.4)-(3.5) can be reduced to the solution of a transcendental equation for σ. Here, we summarize the results of this analysis giving details in appendix A.3.

For $4\pi^2 < d/\mathcal{S} < \tau_{\max}^2$, for which the arch snaps from the compressed flat mode ($\alpha = 0$), analytical insight may be obtained by considering compressions just large enough to obtain

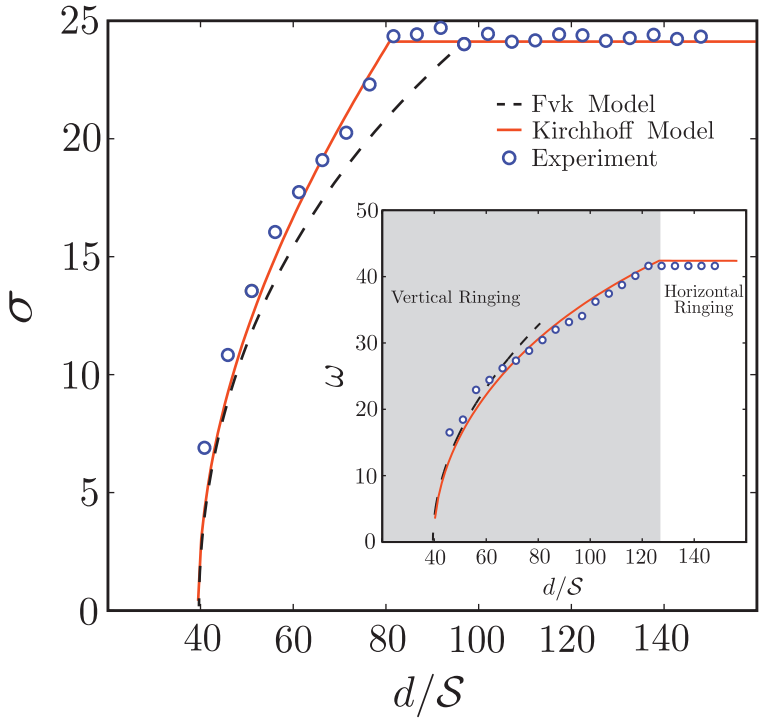

Figure 3.4: Instability growthrate and ringing frequency. Variation of growth rate σ with rescaled lateral confinement, $d/\mathcal{S}$. Inset: The 'ringing' frequency ω as a function of $d/\mathcal{S}$. The results of numerical simulations (solid curve) and experiments (points) are in good agreement with one another and with the prediction of the FvK model (3.6), (3.7) (dashed curve) for $d/\mathcal{S} \approx 4\pi^2$.

buckling, i.e. $(d/\mathcal{S})^{1/2} \gtrsim \tau_0 = 2\pi$. In this limit we find

$$\sigma \approx \frac{4\pi^{3/2}}{\sqrt{3}} \left[\left(\frac{d}{\mathcal{S}} \right)^{1/2} - 2\pi \right]^{1/2} . \tag{3.6}$$

For snap-through from the asymmetric mode ($\alpha = 2$) there is a single eigenvalue of the system, $\sigma \approx 24.113$, that is independent of the end-shortening d and stretchability $\mathcal{S}$. Thus, if we fix $\mathcal{S}$ and increase d starting from $d = 4\pi^2\mathcal{S}$, the growth rate increases monotonically from zero until $d = \tau_{\max}^2\mathcal{S}$, at which point the growth rate plateaus and snap-through happens from the asymmetric mode. Numerical solutions of the Kirchhoff equations confirm a similar picture, though for $d/\mathcal{S} > \tau_{\max}^2$ there is, in fact, a small dependence of σ on $d/\mathcal{S}$, consistent with values reported in a related problem [26].

Experimentally, we tracked the motion of the center of the beam with a high speed camera (Photron FASTCAM APX RS, @3000fps) and performed image analysis with imageJ and

custom MATLAB scripts to study the change in displacement with time. Fig. 3.3 shows that as the center point reaches the base of the arch it rapidly moves from point A to point B, corresponding to the 'snap-through'. The beam then vibrates like an under-damped oscillator about the 'inverted' symmetrical shape before coming to rest. In the inset of fig. 3.3 we plot the absolute value of the central deflection between points A and B; this plot shows that $|w_0|$ grows approximately exponentially with time so that a growth rate can be measured. We non-dimensionalize the experimentally obtained growth rate using the time scale $t_* \sim L^2/ch$ that arises naturally from the dynamic beam equation; fig. 3.4 shows that the time scale of snap-through observed experimentally agrees well with theoretical predictions. In particular, the growth rate σ is strongly dependent on the degree of confinement for $4\pi^2 < d/\mathcal{S} < \tau_{\max}^2$, as predicted by Eqn. (3.6), but once $d/\mathcal{S}$ crosses the critical value $d/\mathcal{S} = \tau_{\max}^2 \approx 80.76$, confinement plays a negligible role and $\sigma \approx 24.113$.

Having snapped away from its unstable configuration, the beam approaches the inverted arch state, which is a stable equilibrium. Since there is little dissipation in our system, the beam oscillates about this state. To understand the 'ringing' frequency $\omega = \sqrt{-\sigma^2}$ of this vibration we perform a linear stability analysis as before, but now with $w_\alpha = w_1$, the stable, first Euler buckling mode. Here, we again see a transition in the form of oscillation based on the quantity $d/\mathcal{S}$. Starting at the critical value $d/\mathcal{S} = 4\pi^2$, as $d/\mathcal{S}$ is increased the ringing frequency of the lowest mode of oscillation increases. The FvK model predicts that

$$\omega \approx \frac{2^{3/2}\pi}{3^{1/2}} \left(\frac{d}{\mathcal{S}} - 4\pi^2 \right)^{1/2} \tag{3.7}$$

for $d/\mathcal{S} \gtrsim 4\pi^2$. The Kirchhoff model confirms this result for $d/\mathcal{S} \approx 4\pi^2$ and shows that ω continues to increase up to $\omega \approx 42.38$ when $d/\mathcal{S} = 122.4$. For $d/\mathcal{S} > 122.4$, the frequency of the lowest mode is fixed at $\omega \approx 42.38$, independent of $d/\mathcal{S}$. We also see a transition in the form of oscillation. For $d/\mathcal{S} < 122.4$, the mode of oscillation with the lowest frequency corresponds to a vertical oscillation, whereas for $d/\mathcal{S} > 122.4$ the mode with lowest frequency also has a significant horizontal component. To compare this picture with experimental data the Fourier transform of the displacement data was taken to measure the frequency of the vibrations after snapping; fig. 3.4 inset shows good agreement between the experiments and theory. The post-snap ringing timescale of the beam ($t_r^{(b)}$) for $d/\mathcal{S} > 122.4$ is governed by the geometry and material properties of the arch:

$$t_r^{(b)} = (2\pi/\omega)t_* \approx 0.148 t_* \approx 0.513 L^2/ch. \tag{3.8}$$

3.7 Ringing of spherical shells

The audible pop that accompanies the snapping of toys, such as jumping discs[15] and the popper shown in fig. 3.1, can be attributed to the ringing frequency. It is therefore natural to compare the ringing timescale (3.8) with that for a spherical cap. The analogue of the beam length for a spherical cap is the base diameter, which we therefore denote by L_{base}. For an elastic spherical cap with radius of curvature R and thickness h, the analogue of the FvK equation (3.1) is the dynamic Donnell–Mushtari–Vlasov equation [32], which reads, in dimensional terms

$$\rho_s h\frac{\partial^2 w}{\partial t^2} + B\nabla^4 w + \frac{Eh}{R^2}w = 0, \quad 0 \le r \le L_{\text{base}}/2, \tag{3.9}$$

where $B = Eh^3/12(1-\nu^2)$ is the appropriate bending stiffness (with Poisson ratio ν), r is the radial coordinate, and we shall assume axisymmetry in what follows. Once a popper has leapt from a table, its edges are free and so the appropriate boundary conditions for (3.9) are $\nabla^2 w|_{r=L_{\text{base}}/2} = \mathrm{d}/\mathrm{d}r(\nabla^2 w)|_{r=L_{\text{base}}/2} = 0$. Performing a linear stability analysis along similar lines to those for the snapping beam (see supplementary information for more details) we obtain the snapping timescale

$$t_r^{(s)} = \frac{\pi}{2}\frac{\sqrt{1-\nu^2}}{\lambda^2}t_*\left(1+\frac{3}{4}\frac{1-\nu^2}{\lambda^4}\frac{L_{\text{base}}^4}{h^2R^2}\right)^{-1/2} \tag{3.10}$$

where $\lambda \approx 3.196$ is an eigenvalue that is found numerically from a solvability condition.

For the majority of the shells of interest here, the term in parentheses in (3.10) is approximately unity and we find, assuming $\nu \approx 1/2$, that $t_r^{(s)} \approx 0.133 t_*$. Remarkably, we find that this result is within 10% of the corresponding result for the ringing frequency of arched beams in (3.8). Given the quantitative robustness of the ringing timescale, it is natural to measure its value in a wide range of experiments combining the snapping shells that motivated our study with the carefully controlled snapping beams. For spherical shells (commercially available toy poppers, bimetallic disks and sections of squash balls) we measure with a microphone the audible 'pop' sound that they make during snapping and extract the dimensional frequency, ω/t_* from this. The lengthscale used to estimate t_* is the uncompressed length L for arches and L_{base} (the diameter of the spherical cap base) for hemispherical shells. Fig. 3.5 shows plots of the experimentally measured ringing timescale, t_r, as a function of the characteristic timescale t_*; this confirms that the prediction of the linear stability analysis for

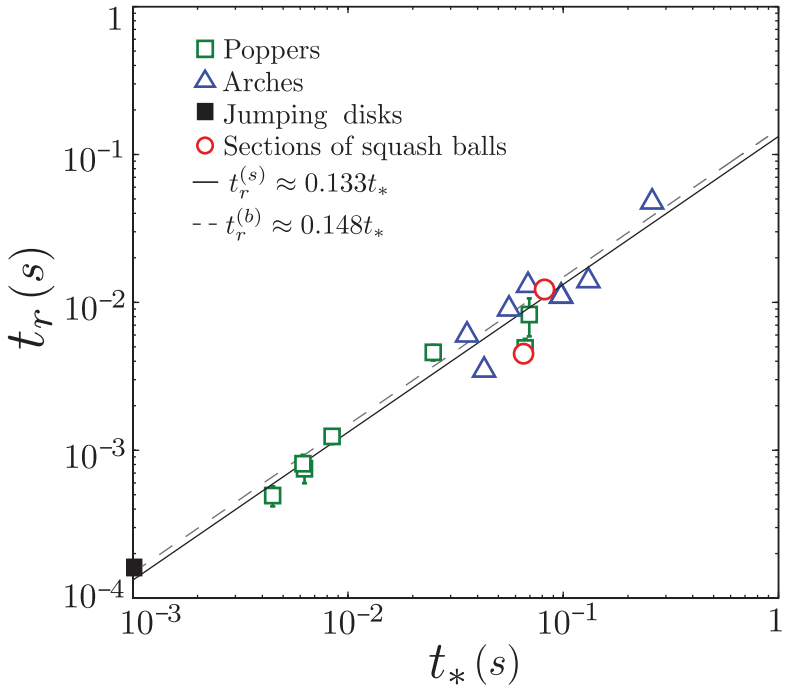

Figure 3.5: Scaling for ringing timescale. The ringing timescale measured experimentally, t_r, scales with the time scale t_* as predicted by our analysis for arches, $t_r^{(b)} \approx 0.148 t_*$ and for hemispherical shells $t_r^{(s)} \approx 0.133 t_*$.

both beams and shells, are in excellent agreement with experiments.

3.8 Discussion

We have studied the dynamic snapping of beams and shells. By first analyzing the quasi-static deformation of a point-loaded beam, we established the key role of stretchability in the small end-end compression regime, and showed that for $4\pi^2\mathcal{S} < d < 80.76\mathcal{S}$ the static deformation and dynamic snapping are fully symmetric, a regime that ceases to exist in the inextensibility limit $S \to 0$. However, we emphasize that this is not a generic feature of such systems; the loading also plays a crucial role since when indenting with a flat wall, the arch remains symmetric throughout the deformation independent of the stretchability [30, 31]. Interestingly, our analysis and experiments showed that stretchability of the beam also plays a key role in determining the timescales that govern both snap-through and ringing. More generally, we found that the characteristic timescale in each case $\sim L^2/ch$, which may be interpreted physically as the timescale for the beam to 'feel' its ends using sound waves of

speed c, augmented by a geometric factor L/h. The augmenting factor, $L/h \sim \mathcal{S}^{-1/2}$, so that for a given stretchability $\mathcal{S}$ it is the time taken to 'feel' the beam ends that limits the dynamics of motion. For shells, we showed that the timescale of ringing scales in the same way with the shell's properties and, moreover, with a very similar prefactor. This allowed us to present a universal description for the audible 'pop' that is a distinctive feature of snapping both in everyday toys and laboratory experiments.

While our results have demonstrated that the ringing of arches and shells are quantitatively similar, many open questions remain to properly understand the dynamics of snapping structures. A particularly interesting open question concerns the effect of finite stretchability in determining the snapping growth rate for shells and whether such effects manifest themselves in terms of the symmetry (or asymmetry) of the snapping mode, as we have seen for snapping beams.

References

[1] J. E. Gordon. *Structures or Why things don't fall down*. Penguin Books Ltd., 1978.

[2] E. Hurlbrink. *Schiffbau*, 9:517, 1908.

[3] S. P. Timoshenko. Buckling of a uniformly compressed circular arch. *Bull. Polytech. Inst. Kiev.*, 1910.

[4] Y.C. Fung and A. Kaplan. Buckling of Low Arches or Curved Beams of Small Curvature. *National Advisory Committee for Aeronautics*, (2840):1–76, 1952.

[5] A. Gjelsvik and S.R. Bodner. The Energy Criterion in Snap Buckling Problems with Application to Clamped Arches. *ASCE Proceedings, Journal of the Engineering Mechanics Division*, 88(5):87–134, 1962.

[6] A. B. Pippard. The elastic arch and its modes of instability. *Eur. J. Phys.*, 11:359–365, 1990.

[7] P. Patrício, M. Adda-Bedia, and M. Ben Amar. An elastica problem: instabilities of an elastic arch. *Physica D*, 124:285–295, 1998.

[8] Y. L. Pi, M. A. Bradford, and B. Uy. In-plane stability of arches. *International Journal of Solids and Structures*, 39(1):105–125, 2002.

[9] R. H. Plaut and L. N. Virgin. Vibration and Snap-Through of Bent Elastica Strips Subjected to End Rotations. *Journal of Applied Mechanics*, 76:041011, 2009.

[10] S. Poppinga and M. Joyeux. Different mechanics of snap-trapping in the two closely related carnivorous plants Dionaea muscipula and Aldrovanda vesiculosa. *Physical Review E*, 84(4), 2011.

[11] Y. Forterre, J. M. Skotheim, J. Dumais, and L. Mahadevan. How the venus flytrap snaps. *Nature*, 433:421–425, 2005.

[12] J. M. Skotheim and L. Mahadevan. Physical limits and design principles for plant and fungal movements. *Science*, 308:1308–1310, 2005.

[13] W. H. Wittrick, D. M. Myers, and W. R. Blunden. Stability of a Bimetallic Disk. *Quart. Journ. Mech. and Applied Math.*, 6:15–31, 1953.

[14] D. R. Lapp. Exploring extreme physics with an inexpensive plastic toy popper. *Phys. Educ.*, 44:492–493, 2008.

[15] C. Ucke and H.-J. Schlichting. Revival of the jumping disc. *Phys. Educ.*, 44:612–617, 2009.

[16] C Hsu and W Hsu. Instability in micromachined curved thermal bimorph structures. *Journal of Micromechanics and Microengineering*, 13(6):955–962, 2003.

[17] K Das and R C Batra. Symmetry breaking, snap-through and pull-in instabilities under dynamic loading of microelectromechanical shallow arches. *Smart Materials and Structures*, 18(11):115008, 2009.

[18] P. Gonçalves. Dynamic non-linear behavior and stability of a ventricular assist device. *International Journal of Solids and Structures*, 40(19):5017–5035, 2003.

[19] D. P. Holmes and A. J. Crosby. Snapping surfaces. *Adv. Matter*, 19:3589–3593, 2007.

[20] C. Xia, H. Lee, and N Fang. Solvent-driven polymeric micro beam device. *Journal of Micromechanics and Microengineering*, 20(8):085030, 2010.

[21] Ajit S Panesar, Kalyan Hazra, and Paul M Weaver. Investigation of thermally induced bistable behaviour for tow-steered laminates. *COMPOSITES PART A*, 43(6):926–934, June 2012.

[22] C Thill, J Etches, I Bond, K Potter, and P Weaver. Morphing skins. *The Aeronautical Journal*, 112(1129):117–139, 2008.

[23] A. Libai and J. G. Simmonds. *The nonlinear theory of elastic shells*. Cambridge University Press, 1998.

[24] J. S. Humphreys. On dynamic snap buckling of shallow arches. *AIAA J.*, 4:878–886, 1966.

[25] Y.-L. Pai and M. A. Bradford. Nonlinear dynamic buckling of pinnedfixed shallow arches under a sudden central concentrated load. *Nonlinear Dyn.*, 73:1289–1306, 2013.

[26] Aurélie Fargette, Sébastien Neukirch, and Arnaud Antkowiak. Elastocapillary snapping: Capillarity induces snap-through instabilities in small elastic beams. *Phys. Rev. Lett.*, 112:137802, Apr 2014.

[27] B. Audoly and Y. Pomeau. *Elasticity and Geometry*. Oxford University Press, 2010.

[28] Goriely A. Neukirch S., Frelat J. and Maurini C. Vibrations of post-buckled rods: the singular inextensible limit. *J. Sound Vib.*, 331:704–720, 2012.

[29] Roman B. Hure J. and Bico J. Stamping and wrinkling of elastic plates. *Phys. Rev. Lett.*, 109(054302), 2012.

[30] Roman B. and Pocheau A. Buckling cascade of thin plates: Forms, constraints and similarity. *Europhys. Lett.*, 46(5):602–608, 1999.

[31] Roman B. and Pocheau A. Postbuckling of bilaterally constrained rectangular thin plates. *J. Mech. Phys. Solids*, 50:2379–2401, 2002.

[32] Soedel W. *Vibrations of Shells and Plates*. Marcel Dekker, 2004.

Chapter 4

Summary

In this thesis, we have discussed the response of soft polymeric structures under two seemingly different stimuli. For swelling induced deformations, percolation of fluid droplet inside an elastic network leads to bending or creasing of a clamped elastomer beam. Whereas, poking a soft, elastic arch leads to its global stability loss and subsequent jumping to a stable state far from the initial configuration. A very natural extension is to combine the knowledge of swelling and snapping to study 'swelling induced snap buckling', a process that can be incorporated as a switch in biomimetic, functional devices. Fig. 4.1 describes the process, droplet of a favorable solvent on a clamped elastomeric arch causes it to snap upward. In chapter 2, we have showed that the swelling stress developed inside an elastomeric network depends on type and volume of solvent. For lower values of initial curvature and thickness this swelling stress would be high enough to overcome the bending strain energy of the arch and make it snap. We expect the timescale of snap to be independent of the stimulus and purely geometric. Understanding of this coupled problem would be a significant step in using elastic instabilities for form and function.

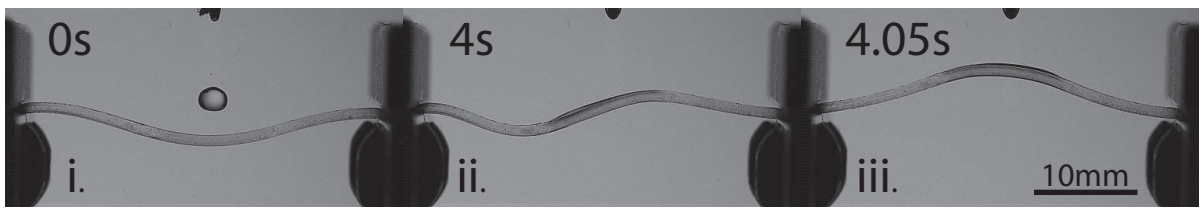

Figure 4.1: Swelling induced snap buckling of a clamped Polydimethylsiloxane (PDMS) arch.

Appendix A

Analytical Formulation for Snapping

Here we give details of the analytical results that can be obtained for the snapping problem by using the Föppl-von-Kármán equations, and compares these with the results obtained by using the non-linear Kirchhoff equations. We begin by presenting the Föppl-von-Kármán (FvK) results along with an outline of their derivation. We also present a derivation of the ringing timescale of a spherical cap based on the Donnell-Mushtari-Vlasov equations.

A.1 Problem setup

The setup we consider is shown in figure A.1. The geometrical parameters of the beam are its length L, thickness h and width b into the page; the height of the center of the beam (measured relative to the clamped ends) is $w_0 = w(0)$. The mechanical properties of the beam are its Young's modulus, E, Poisson ratio ν and density ρ_s. The modulus E often appears in combination with the thickness h and beam width b to give the bending stiffness

$$B = \frac{Eh^3 b}{12}. \tag{A.1}$$

Note that because we are considering a thin strip rather than an infinitely wide plate there is no factor of $1 - \nu^2$ in the denominator here [see 1, for example].

Under the assumptions of small slopes made in the derivation of the FvK equations, the following dynamic beam equation describes the profile $w(x, t)$ of a beam in response to a

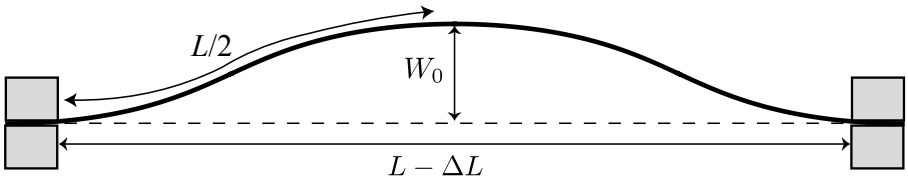

Figure A.1: The notation used for the geometry of a beam of length L, which is clamped at its ends.

point force F acting at the origin:

$$\rho_s bh\frac{\partial^2 w}{\partial t^2} + B\frac{\partial^4 w}{\partial x^4} + T\frac{\partial^2 w}{\partial x^2} = F\delta(x). \tag{A.2}$$

Here T is the compressive force applied, which is related to the strain in the x direction, ϵ_{xx}, by Hooke's law $\epsilon_{xx} = -T/Ehb$. The strain ϵ_{xx} is also related to the horizontal and vertical displacements u and w, respectively, by

$$\epsilon_{xx} = \frac{\partial u}{\partial x} + \tfrac{1}{2}\left(\frac{\partial w}{\partial x}\right)^2. \tag{A.3}$$

We therefore have that

$$-\frac{T}{Ehb} = \frac{\partial u}{\partial x} + \tfrac{1}{2}\left(\frac{\partial w}{\partial x}\right)^2. \tag{A.4}$$

The two equations (A.2) and (A.4) are to be solved with the boundary conditions

$$w(\pm L/2) = w'(\pm L/2) = 0, \quad u(\pm L/2) = \mp\Delta L/2. \tag{A.5}$$

When the beam is in contact with the indentor, one can either prescribe a fixed load or a fixed displacement. Here we adopt the latter approach; we impose the condition $w(0) = w_0$, which provides an additional condition that allows the required force F to be determined.

To non-dimensionalize the problem, we scale lengths by the length of the beam, L, and introduce dimensionless variables $w' = w/L$, $x' = x/L$, etc. Since the delta function has units $1/[L]$ it is natural then to introduce the dimensionless indentation force $f = F \times L^2/B$. Time is scaled by $t_* = L^2\left(\rho_s hb/B\right)^{1/2}$, i.e. we introduce $t' = t/t_*$. Note that this time scale can be written as $t_* = 2\sqrt{3}\frac{L}{c}\frac{L}{h}$, where $c = (E/\rho)^{1/2}$ is the speed of sound in the material.

Inserting these scalings into (A.2) and (A.4) (and dropping primes henceforth) we have

$$\frac{\partial^2 w}{\partial t^2} + \frac{\partial^4 w}{\partial x^4} + \tau^2 \frac{\partial^2 w}{\partial x^2} = f\delta(x) \tag{A.6}$$

and

$$-\mathcal{S}\tau^2 = \frac{\partial u}{\partial x} + \tfrac{1}{2}\left(\frac{\partial w}{\partial x}\right)^2 \tag{A.7}$$

where $\tau^2 = TL^2/B$ is the dimensionless compression force and

$$\mathcal{S} = \frac{B}{EhL^2 b} = \frac{h^2}{12L^2} \tag{A.8}$$

is the dimensionless 'stretchability' for reasons that shall shortly become apparent. The boundary conditions (A.5) have the obvious forms, though it is worth noting that the condition on the displacement u becomes

$$u(\pm 1/2) = \mp d/2 \tag{A.9}$$

where $d = \Delta L/L$ is the ratio of end shortening to the length of the beam.

We note that upon integrating (A.7) over $-1/2 \leq x \leq 1/2$ and applying (A.9) we have

$$\int_{-1/2}^{1/2} \left(\frac{\partial w}{\partial x}\right)^2 \mathrm{d}x = 2\left(d - \mathcal{S}\tau^2\right). \tag{A.10}$$

Geometrically speaking, this equation shows how the amplitude of the beam deformation must be chosen to accommodate the imposed end-shortening d. However, the presence of a non-zero stretchability, $\mathcal{S}$, reduces the effective amount of end-shortening felt by the beam and hence reduces the amplitude of its deformation. The factor $\mathcal{S}$ therefore represents the propensity of the beam to compress/stretch in response to externally applied stresses.

A.2 Statics

To simplify the analysis, we begin by neglecting the time derivatives that appears in (A.6). This corresponds to the assumption that the loading of the arch occurs quasistatically. In

this limit the partial derivatives all become ordinary x-derivatives and (A.6) becomes

$$\frac{\mathrm{d}^4 w}{\mathrm{d}x^4} + \tau^2 \frac{\mathrm{d}^2 w}{\mathrm{d}x^2} = f\delta(x), \tag{A.11}$$

Considering each of the intervals $-1/2 \le x < 0$ and $0 < x < 1/2$ separately, we have

$$\frac{\mathrm{d}^4 w}{\mathrm{d}x^4} + \tau^2 \frac{\mathrm{d}^2 w}{\mathrm{d}x^2} = 0 \ \text{ on } \ -1/2 \le x < 0, \quad 0 < x < 1/2 \tag{A.12}$$

subject to the boundary conditions

$$w(\pm 1/2) = w'(\pm 1/2) = 0, \quad w(0) = w_0, \quad [w]^+_- = [w']^+_- = [w'']^+_- = 0, \ \ [w''']^+_- = f \tag{A.13}$$

and the imposed confinement

$$2(d - \tau^2 \mathcal{S}) = \int_{-1/2}^{1/2} \left(\frac{\mathrm{d}w}{\mathrm{d}x}\right)^2 \mathrm{d}x. \tag{A.14}$$

Here $[g]^+_- \equiv g(0^+) - g(0^-)$ denotes the discontinuity in the quantity g across the indentation point $x = 0$.

The general solution of (A.12) may be written

$$w(x) = \begin{cases} A_- + B_- x + C_- \cos \tau x + D_- \sin \tau x, & -1/2 < x < 0 \\ A_+ + B_+ x + C_+ \cos \tau x + D_+ \sin \tau x, & 0 < x < 1/2. \end{cases} \tag{A.15}$$

The continuity of w'' at $x = 0$ gives immediately that $C_- = C_+ = C$. In turn, the continuity of w at $x = 0$ gives that $A_- = A_+ = A$ and, further, that

$$A + C = w_0. \tag{A.16}$$

The clamped boundary conditions give

$$0 = A \pm B_\pm/2 + C \cos \tau/2 \pm D_\pm \sin \tau/2 \tag{A.17}$$

and

$$0 = B_\pm \mp C\tau \sin \tau/2 + D_\pm \tau \cos \tau/2. \tag{A.18}$$

Hence

$$(B_+ + B_-)/2 + (D_+ + D_-)\sin\tau/2 = 0 \tag{A.19}$$

and

$$B_+ + B_- + (D_+ + D_-)\tau\cos\tau/2 = 0 \tag{A.20}$$

so that either

$$D_+ + D_- = 0, \quad B_+ + B_- = 0 \tag{A.21}$$

or

$$\tan\tau/2 = \tau/2. \tag{A.22}$$

Note that the first possibility corresponds to a symmetric mode of deformation since B and D multiply the odd terms in $w(x)$. The latter possibility corresponds to an asymmetric mode (but *not* antisymmetric). We need to consider each of these possibilities separately.

A.2.1 The symmetric mode

In the symmetric mode we satisfy (A.21) by letting

$$D_+ = -D_- = D, \quad B_+ = -B_- = B. \tag{A.23}$$

It is then a simple matter to see that (A.15) is the symmetric shape

$$w(x) = A + B|x| + C\cos\tau x + D\sin\tau|x|, \quad -1/2 < x < 1/2. \tag{A.24}$$

Using the imposed displacement and slope conditions at $x = 0$ along with the clamped conditions at $x = 1/2$ we find that

$$A = w_0\frac{1 - \cos\tau/2 - \tau/2\sin\tau/2}{2 - 2\cos\tau/2 - \tau/2\sin\tau/2} \tag{A.25}$$

$$B = w_0\frac{\tau\sin\tau/2}{2 - 2\cos\tau/2 - \tau/2\sin\tau/2} \tag{A.26}$$

$$C = w_0\frac{1 - \cos\tau/2}{2 - 2\cos\tau/2 - \tau/2\sin\tau/2} \tag{A.27}$$

$$D = -w_0\frac{\sin\tau/2}{2 - 2\cos\tau/2 - \tau/2\sin\tau/2}. \tag{A.28}$$

The shape is thus determined, although we currently do not have any indication of the value of τ. To determine this quantity, we need to make use of the given end-end displacement, d. By definition we have that

$$d - \tau^2 \mathcal{S} = \int_{-1/2}^{1/2} \tfrac{1}{2} w_x^2 \, \mathrm{d}x = \int_0^{1/2} w_x^2 \, \mathrm{d}x = w_0^2 \frac{\tau \left(2\tau + \tau \cos \tau/2 - 6 \sin \tau/2\right)}{\left(\tau \cos \tau/4 - 4 \sin \tau/4\right)^2}. \tag{A.29}$$

This shows that for a given value of d, w_0 may be written parametrically in terms of τ as

$$w_0^2 = (d - \tau^2 \mathcal{S}) \frac{\left(\tau \cos \tau/4 - 4 \sin \tau/4\right)^2}{\tau \left(2\tau + \tau \cos \tau/2 - 6 \sin \tau/2\right)}. \tag{A.30}$$

Before any indentation occurs, the shape is given by $w = \frac{w_0}{2}(1 + \cos 2\pi x)$, which corresponds to $\tau = 2\pi$ giving $w_0 = 2(d - 4\pi^2 \mathcal{S})^{1/2}/\pi$. Also, the right hand side of (A.30) is a decreasing function of $\tau \geq 0$ so that, as indentation progresses (i.e. as w_0 decreases) τ must increase. We therefore expect that the value of τ should increase up until the point at which either $\tau/4 = \tan \tau/4$ (so that $\tau \approx 17.97$) or until $\tau = (d/\mathcal{S})^{1/2}$. In either one of these cases $w_0 = 0$. However, since the asymmetric mode has $\tau = \tau_{\max} \approx 8.99$ (the solution of $\tau_{\max}/2 = \tan \tau_{\max}/2$) there is also the possibility that the symmetric solution is replaced by the asymmetric one at a displacement

$$w_0^{(c)} \approx 0.62(d - 80.76\mathcal{S})^{1/2}. \tag{A.31}$$

Now, in the symmetric mode the indentation force is given by

$$f = [w''']_-^+ = -2\tau^3 D = 2w_0 \frac{\tau^3 \sin \tau/2}{2 - 2\cos \tau/2 - \tau/2 \sin \tau/2}. \tag{A.32}$$

Because of the nonlinear relationship between the displacement w_0 and τ in (A.30), the force law (A.32) is, in general, a nonlinear function of the displacement w_0. However, we note that at the displacement $w_0^{(c)}$ the force is given by $f^{(c)} \approx -207.75 w_0^{(c)}$.

A.2.2 The asymmetric mode

In the asymmetric mode, we have that the compression $\tau = \tau_{\max} \approx 8.99$ where $\tau_{\max}$ is the smallest solution of the equation $\tau_{\max}/2 = \tan(\tau_{\max}/2)$. Returning to the equations for the

unknown coefficients and replacing $\sin(\tau_{\max}/2)$ by $\cos(\tau_{\max}/2)\tau_{\max}/2$ we have

$$\begin{aligned} A + C &= w_0 \\ A \pm B_\pm/2 + C\cos\tau_{\max}/2 \pm D_\pm\tau_{\max}/2\cos\tau_{\max}/2 &= 0 \\ B_\pm \mp C\tau_{\max}^2/2\cos\tau_{\max}/2 + D_\pm\tau_{\max}\cos\tau_{\max}/2 &= 0 \\ (B_+ + B_-) + (D_+ + D_-)\tau_{\max}\cos\tau_{\max}/2 &= 0, \end{aligned}$$

noting that the third of these equations implies the fourth. We find

$$A + C(1 + \tau_{\max}^2/4)\cos\tau_{\max}/2 = 0 \tag{A.33}$$

and so

$$A = -w_0\frac{(1+\tau_{\max}^2/4)\cos\tau_{\max}/2}{1-(1+\tau_{\max}^2/4)\cos\tau_{\max}/2}, \quad C = \frac{w_0}{1-(1+\tau_{\max}^2/4)\cos\tau_{\max}/2}. \tag{A.34}$$

The requirement that the first derivative is continuous at the indentation point implies

$$B_- + D_-\tau = B_+ + D_+\tau. \tag{A.35}$$

Since we have already used the continuity of w'' at $x = 0$ to determine C the only remaining relationship comes from the imposed confinement, d. As it is clear that the coefficients $B_\pm, D_\pm \propto w_0$, it is convenient to write

$$\frac{d - \tau_{\max}^2\mathcal{S}}{w_0^2} = \frac{1}{2}\int_{-1/2}^{1/2}\omega_x^2\,\mathrm{d}x \tag{A.36}$$

where $\omega = w/w_0$. In this expression, it is possible to express D_+/w_0, $B_\pm/w_0$ in terms of D_-/w_0 and thereby determine these coefficients as w_0 varies for a given value of d by solving (A.36) numerically. This is useful for determining the predicted shape of the beam. However, our main interest lies in understanding the force as a function of displacement and, possibly the bending energy of a given deformation. In this regard, we have that the indentation force is given by

$$f = [w''']_-^+ = -\tau_{\max}^3(D_+ - D_-). \tag{A.37}$$

The quantity of most interest then is $D_+ - D_-$, which can be written

$$D_+ - D_- = -C\frac{\tau_{\max}\cos\tau_{\max}/2}{1-\cos\tau_{\max}/2}. \tag{A.38}$$

Hence

$$f = \alpha(\tau_{\max})w_0 \tag{A.39}$$

where

$$\alpha(\tau_{\max}) = \frac{\tau_{\max}^4\cos\tau_{\max}/2}{2-(2+\tau_{\max}^2/4)\cos\tau_{\max}/2} \approx -207.75$$

is a constant, independent of the value of d. We note that the force in this regime is therefore linearly proportional to w_0. We see that this force decreases as the amount of indentation approaches $w_0 = 0$ (i.e. as the bump approaches the second Euler buckling mode).

A.2.3 Transition from symmetric to asymmetric modes

To determine when the transition from symmetric to asymmetric occurs, we compare the energies of the two different configurations. We note that, by construction, the imposed compression, d, is the same in both configurations and so the stretching energy must be constant. To simplify the calculation further, we note that integrating (A.10) by parts and using (A.6) gives

$$2(d-\mathcal{S}\tau^2) = \int_{-1/2}^{1/2} w_x^2\,\mathrm{d}x = \tau^{-2}\int_{-1/2}^{1/2}[w_{4x} - f\delta(x)]w\,\mathrm{d}x \tag{A.40}$$

so that

$$2\tau^2(d-\mathcal{S}\tau^2) = -fw_0 + \int_{-1/2}^{1/2} w_{xx}^2\,\mathrm{d}x = -fw_0 + 2U_B \tag{A.41}$$

and thus

$$U_B = w_0 f/2 + \tau^2(d-\mathcal{S}\tau^2). \tag{A.42}$$

This relationship holds whichever mode (symmetric or asymmetric) the system is in. However, where both modes exist for a given value of w_0, the asymmetric mode has both a lower force f and a lower value of the compression τ than the symmetric mode. It is therefore clear from (A.42) that, when the asymmetric mode exists, it has a lower bending energy (and so should be expected to be observed in preference to) the symmetric mode.

To summarize, there are two classes of solutions: symmetric and asymmetric. Also, as (A.14) implies the requirement that $d - \tau^2\mathcal{S} \geq 0$, the form of solution is different based on the quantity $d/\mathcal{S}$, which is fixed for any given experiment. The initial buckling of the beam occurs in the symmetric state and corresponds to $\tau = 2\pi$. Thus, if $d/\mathcal{S} < 4\pi^2$, there is no buckling, i.e. the compressed flat state is the only solution, and $d = 4\pi^2\mathcal{S}$ defines the critical shortening required to give buckling.

In the asymmetric state, $\tau = \tau_{\max} \approx 8.99$ (the smallest solution of $\tau_{\max}/2 = \tan \tau_{\max}/2$) is fixed independent of w_0 or f. Hence if $4\pi^2 < d/\mathcal{S} < \tau_{\max}^2$, the asymmetric solution does not exist, and the symmetric mode must be observed throughout indentation, even until $w_0 = 0$, at which point we reach the second buckling mode of the beam and so $f = 0$ also.

In the case $d/\mathcal{S} > \tau_{\max}^2$, both symmetric and asymmetric solutions can be present, depending on w_0. For small indentations, $\tau \approx 2\pi$ and only the symmetric solution exists. As the indentation progresses, w_0 decreases to $w_0^{(c)} \approx 0.624(d - 80.76\mathcal{S})^{1/2}$ while τ increases to $\tau_{\max}$. Beyond this point both modes exist, but the asymmetric mode is energetically favourable. Thus the shape transitions to the asymmetric mode at $w_0 = w_0^{(c)}$ and remains in an asymmetric state as the midpoint is indented from $w_0 = w_0^{(c)}$ to $w_0 = 0$.

If $d/\mathcal{S} \geq 80.76$ then we observe two different modes:

- the symmetric mode for

$$0.62(d - 80.76\mathcal{S})^{1/2} \leq w_0 \leq 2(d - 4\pi^2\mathcal{S})^{1/2}/\pi$$

- the asymmetric mode for

$$0 \leq w_0 \leq 0.62(d - 80.76\mathcal{S})^{1/2}$$

If $4\pi^2 \leq d/\mathcal{S} \leq 80.76$ we observe only the symmetric mode. The corresponding force laws are

$$f = \begin{cases} g[\tau(w_0)]\ w_0, & \text{symmetric mode,} \\ -207.75\ w_0, & \text{asymmetric mode,} \end{cases} \tag{A.43}$$

where

$$g(\tau) = \frac{2\tau^3 \sin \tau/2}{2 - 2\cos \tau/2 - \tau/2 \sin \tau/2} \tag{A.44}$$

and τ satisfies

$$w_0 = (d - \tau^2\mathcal{S})^{1/2}\frac{\tau\cos\tau/4 - 4\sin\tau/4}{\tau^{1/2}\left(2\tau + \tau\cos\tau/2 - 6\sin\tau/2\right)^{1/2}}. \tag{A.45}$$

It is interesting to note that the second part of the force law in (A.43) is universal and does not depend on the values of either d or $\mathcal{S}$.

Finally, we note that the maximum force observed is that at the transition between symmetric and asymmetric modes, i.e.

$$f^{(c)} = -207.75\ w_0^{(c)} = -129.53(d - 80.76\mathcal{S})^{1/2}. \tag{A.46}$$

A.3 Dynamics

We now want to explore the snap-through dynamics. As we have established above, the form of equilibrium deformation depends on the quantity $d/\mathcal{S}$. If $d/\mathcal{S} < 4\pi^2$, the flat compressed state is stable, and clearly there is no snapping. For $4\pi^2 < d/\mathcal{S} < \tau_{\max}^2$, the solution corresponding to $w_0 = f = 0$ is the flat, compressed but unstable beam, whereas if $d/\mathcal{S} > \tau_{\max}^2$, the $w_0 = f = 0$ solution is the unstable, antisymmetric (mode 2) solution of an end-shortened beam with no applied force.

In either case, the fact that the force vanishes at this point, combined with the fact that these solutions are unstable (to be shown subsequently), suggests that snap-through occurs at this point. Alternatively, from the analysis above we see immediately that if the indentation were to continue for $w_0 < 0$ then the vertical force would have to become negative: this corresponds to an attractive interaction between the indentor and the beam and, assuming no such adhesive attraction exists, is not possible. Therefore snap-through must occur.

To explore this snap-through, we study the dynamic problem. In both cases, the snap-through takes the system from an unstable state with $w_0 = 0$ to the stable, symmetric solution, i.e. the inverted form of the initially arched beam. Since the applied force due to the indentor plays no role in the dynamics, we can examine the timescale of snap-through by investigating the linear stability of both of the states with $w_0 = 0$ and determining the growth rate of the instability, σ. We can also investigate the ringing frequency of the beam once it reaches the inverted state via a linear stability analysis of the stable, symmetric arched beam.

A.3.1 Linear stability analysis of snapping

Once contact is lost with the indentor, the evolution of the beam shape during snapping is governed by (A.6) with $f = 0$, i.e.

$$\frac{\partial^2 w}{\partial t^2} + \frac{\partial^4 w}{\partial x^4} + \tau^2 \frac{\partial^2 w}{\partial x^2} = 0. \tag{A.47}$$

We look for a solution of the form $w(x,t) = w_\alpha(x) + \epsilon w_p(x) e^{\sigma t}$, $\tau = \tau_\alpha + \epsilon \tau_p e^{\sigma t}$. Here, $w_\alpha(x)$ is the unperturbed shape ($\alpha = 0, 2$ depending on whether this is the mode 0 or mode 2 state) and τ_α is the corresponding compression. $w_p(x)$ and τ_p are the perturbations to the shape and compression, respectively. At $O(\epsilon)$, we have the following ODE for $w_p(x)$

$$\frac{\mathrm{d}^4 w_p}{\mathrm{d}x^4} + \tau_\alpha^2 \frac{\mathrm{d}^2 w_p}{\mathrm{d}x^2} + \sigma^2 w_p = -2\tau_\alpha \tau_p \frac{\mathrm{d}^2 w_\alpha}{\mathrm{d}x^2}, \tag{A.48}$$

which should satisfy the boundary conditions $w_p = w_p' = 0$ at $x = \pm 1/2$ as well as the length constraint given by expanding (A.14) to $O(\epsilon)$

$$\int_{-1/2}^{1/2} \frac{\mathrm{d}w_\alpha}{\mathrm{d}x} \frac{\mathrm{d}w_p}{\mathrm{d}x} \, \mathrm{d}x = -2\mathcal{S}\tau_\alpha \tau_p. \tag{A.49}$$

It might reasonably be expected that the function $w_p(x)$ will be an even function of x since it has to get the beam 'close' to the symmetrical inverted beam shape. From this expectation, (A.49) shows that in the case of snap-through from the (odd) mode 2 state, the integrand in (A.49) is odd, and so the LHS is zero and thus τ_p must equal 0. A detailed calculation shows that this heuristic expectation is, in fact correct, and that $\tau_p = 0$ to within numerical errors. We therefore make this assumption in the analysis that follows to clarify the presentation. For snap-through from the flat mode 0 state (the compressed state), $w_0 \equiv 0$ and so we immediately have that $\tau_p = 0$ in this case too. We shall therefore assume that $\tau_p = 0$ in what follows; repeating the calculation without either this assumption or that of the evenness of w_p confirms that both of these assumptions are in fact valid.

Seeking a symmetric solution of (A.48) we find that the growth rate σ must be such that

$$\lambda_+ \tan \lambda_+ = \lambda_- \tan \lambda_- \tag{A.50}$$

where

$$\lambda_{\pm}^2 = \tfrac{1}{8}\left[\tau_\alpha^2 \pm (\tau_\alpha^4 - 4\sigma^2)^{1/2}\right]. \tag{A.51}$$

For snap-through from the mode 2 Euler buckling solution, i.e. $\tau_\alpha = \tau_{\max}$, we find that the system has a single eigenvalue, $\sigma \approx 24.11$. We note that this value is independent of the end-shortening d and stretchability $\mathcal{S}$.

For snap-through from the mode 0 compressed solution, the value of τ about which we are linearizing is that for which $w_0 \equiv 0$, i.e. $\tau_\alpha = (d/\mathcal{S})^{1/2}$. The value of σ as a function of $d/\mathcal{S}$ can be determined numerically. However, for $\tau_\alpha \approx 2\pi$, i.e. close to the critical compression required for arch buckling, we expect that the snap-through instability should disappear. By letting $(d/\mathcal{S})^{1/2} = \tau_\alpha = 2\pi + \epsilon$ with $\epsilon \ll 1$ and expanding (A.50) as a power series in ϵ we find that $\sigma \approx 4\pi^{3/2}/\sqrt{3}\epsilon^{1/2}$; we therefore have

$$\sigma \approx \frac{4\pi^{3/2}}{\sqrt{3}}\left[\left(\frac{d}{\mathcal{S}}\right)^{1/2} - 2\pi\right]^{1/2}. \tag{A.52}$$

Thus we see that the growth rate of the zeroth mode does depend on the amount of end-shorterning d, increasing from 0 when $d/\mathcal{S} = 4\pi^2$ and the compressed state is unstable.

A.3.2 Linear stability analysis of ringing

The previous analysis gives a characteristic time scale for the snap-through instability. To compute the frequency of the 'ringing' that is observed after snap-through we must perform a similar analysis but for a perturbation about the first buckling mode, i.e. we let $w(x,t) = w_1(x) + \epsilon w_p(x)e^{\sigma t}$, $\tau = \tau_1 + \epsilon\tau_p e^{\sigma t}$ where

$$w_1(x) = \alpha(1 + \cos 2\pi x) \tag{A.53}$$

$\alpha = -\left(\frac{d}{\pi^2} - 4\mathcal{S}\right)^{1/2}$ and $\tau_1 = 2\pi$.

We find that

$$\begin{aligned}\frac{w_p(x)}{\alpha} = \frac{16\pi^3}{\sigma^2}\tau_p \cos 2\pi x \quad &+ \quad A\cosh\left[\lambda_-(x+1/2)\right] + B\sinh\left[\lambda_-(x+1/2)\right] \\ &+ \quad C\cos\left[\lambda_+(x+1/2)\right] + D\sin\left[\lambda_+(x+1/2)\right]\end{aligned}$$

where

$$\lambda_{\pm} = \left[\left(4\pi^4 - \sigma^2\right)^{1/2} \pm 2\pi^2\right]^{1/2}. \tag{A.54}$$

The unknowns τ_p, σ, A, B, C and D are determined as an eigenproblem based on the boundary conditions

$$w_p(\pm 1/2) = w_p'(\pm 1/2) = 0 \tag{A.55}$$

and integrated Hooke's law

$$2\tau_p \mathcal{S} - \alpha \int_{-1/2}^{1/2} \frac{\mathrm{d}w_p}{\mathrm{d}x} \sin 2\pi x \; \mathrm{d}x = 0 \tag{A.56}$$

with eigenvalue σ^2. This eigenproblem can easily be solved numerically.

For all values of $d/\mathcal{S} > 4\pi^2$ we find the eigenvalue $\sigma^2 \approx -1968.05$, i.e. the solution is stable, and the perturbation gives an oscillation with dimensionless frequency $\omega = \sqrt{-\sigma^2} \approx 44.36$. In this case, the eigenfunction $w_p(x)$ is an odd function of x and so the combined behaviour gives the illusion of a horizontally oscillating mode, even though the perturbation is only an up-down oscillation.

Another eigenvalue exists, which does depend on the value of $d/\mathcal{S}$. The eigensolution associated with this eigenvalue is even and corresponds to the up-down oscillation that is observed experimentally. For $d/\mathcal{S} - 4\pi^2 \ll 1$ we find that this mode has

$$\sigma^2 \approx -\frac{8\pi^2}{3}\left(\frac{d}{\mathcal{S}} - 4\pi^2\right). \tag{A.57}$$

Alternatively, the ringing frequency $\omega = \sqrt{-\sigma^2}$ is given by

$$\omega = \frac{2^{3/2}\pi}{3^{1/2}}\left(\frac{d}{\mathcal{S}} - 4\pi^2\right)^{1/2}, \tag{A.58}$$

which is in agreement with the numerically-determined predictions of both the FvK and Kirchhoff models.

A.4 Kirchhoff equations

The beam equations we have analysed are derived under the assumption that slopes are small, i.e. $|w_x| \ll 1$. As we are primarily interested in shallow arches and the effect of stretchability, the linear equations capture the experimental observations very well. Moreover, as we have shown, working in the linear regime enables us to obtain analytical formulas and key parameter values. Next, for comparison, and in an attempt to obtain the most accurate prediction of dynamical growth rates possible, we model the problem using the nonlinear Kirchhoff equations.

We consider an extensible beam with centerline $\mathbf{r}(S) = x(S)\mathbf{e}_x + y(S)\mathbf{e}_y$ such that S is the arclength in the reference (stress-free) configuration. Letting s denote the arclength in the current configuration, we define the axial stretch

$$\alpha = \alpha(S) = \frac{ds}{dS} \tag{A.59}$$

To describe the geometry, it is convenient to define θ as the angle between the tangent to the centerline and the horizontal x-direction. Then we have

$$\begin{aligned} \frac{\partial x}{\partial S} &= \alpha \cos\theta \\ \frac{\partial y}{\partial S} &= \alpha \sin\theta, \end{aligned} \tag{A.60}$$

where prime denotes differentiation with respect to S. To describe the mechanics, let $\mathbf{n} = n_x\mathbf{e}_x + n_y\mathbf{e}_y$ be the resultant force and $\mathbf{m} = m\mathbf{e_z}$ the resultant moment attached to the centerline by averaging the stress over the cross section. Balancing linear and angular momentum yields

$$\begin{aligned} &\frac{\partial n_x}{\partial S} = \rho h b \frac{\partial^2 x}{\partial t^2} \\ &\frac{\partial n_y}{\partial S} - F\delta(S - S_c) = \rho h b \frac{\partial^2 y}{\partial t^2}, \quad x(S_c) = 0 \\ &\frac{\partial m}{\partial S} + \alpha(n_x \sin\theta - n_y \cos\theta) = 0. \end{aligned} \tag{A.61}$$

Here the delta function signifies that the force is applied at the (unknown) material point S_c that corresponds to the fixed point $x = 0$ in the lab frame. To close the system, we

must provide two constitutive laws and boundary conditions. We assume a quadratic strain energy, so that the moment is linearly related to the curvature by

$$m = B\theta', \tag{A.62}$$

where B is the bending stiffness as defined in Equation (A.1). For an extensible beam, we also require a constitutive law relating the axial force to the stretch, which reads

$$n_x \cos\theta + n_y \sin\theta = Ehb(\alpha - 1). \tag{A.63}$$

Note that $n_x \cos\theta + n_y \sin\theta$ is the tangential component of the force vector $\mathbf{n}$, thus (A.63) essentially expresses Hooke's law. The clamped boundary conditions are expressed as

$$x(\pm L/2) = \pm L/2 \mp \Delta L/2, \quad y(\pm L/2) = 0, \quad \theta(\pm L/2) = 0, \tag{A.64}$$

and the fixed displacement condition reads $y(S_c) = y_0$, where y_0 is the fixed height at the point of the indentor (equal to w_0 in the FvK analysis).

We next non-dimensionalize the system. We scale lengths by L, so that $S' = S/L$, $x' = x/L$, $y' = y/L$, the force $\mathbf{n}$ by $N = B/L^2$, moment m by $M = B/L$, and as before we introduce the dimensionless force $f = F \times L^2/B$ and we again scale time by $t_* = L^2 (\rho hb/B)^{1/2}$. Inserting the scalings and dropping the primes, the system is

$$\begin{aligned}
&\frac{\partial x}{\partial S} = \alpha\cos\theta, \quad \frac{\partial y}{\partial S} = \alpha\sin\theta \\
&\frac{\partial n_x}{\partial S} = \frac{\partial^2 x}{\partial t^2} \\
&\frac{\partial n_y}{\partial S} - f\delta(S - S_c) = \frac{\partial^2 y}{\partial t^2}, \quad x(S_c) = 0, \quad y(S_c) = y_0 \\
&\frac{\partial m}{\partial S} + \alpha(n_x \sin\theta - n_y \cos\theta) = 0 \\
&m = \frac{\partial \theta}{\partial S} \\
&\mathcal{S}(n_x \cos\theta + n_y \sin\theta) = \alpha - 1,
\end{aligned} \tag{A.65}$$

where the stretching stiffness $\mathcal{S} = h^2/12L^2$ is as defined in the FvK analysis (A.8). The

boundary conditions become

$$x(\pm 1/2) = \pm 1/2 \mp d/2, \quad y(\pm 1/2) = 0, \quad \theta(\pm 1/2) = 0. \tag{A.66}$$

A.4.1 Statics

To study the static deformation of the beam, we drop time derivatives in (A.65). We have solved the resulting system via a shooting method. Starting at $S = -1/2$, we integrate the system forward with shooting variables

$$\mathcal{V} = \{n_x, n_y(-1/2), m(-1/2), f, S_c\}, \tag{A.67}$$

noting that the indentor force implies a jump in n_y at $S = S_c$. The conditions for a successful solution are $x(1/2) = (1-d)/2$, $y(1/2) = 0$, $\theta(1/2) = 0$, along with the conditions at the indentor $x(S_c) = 0$, $y(S_c) = y_0$; the shooting variables $\mathcal{V}$ are iterated on until these five conditions are met.

A.4.2 Upper bound on arch height

Using the Kirchhoff model, we can also determine a limit on the range of arch heights for which the indentation experiment is possible. At a critical arch height (or critical end displacement $d_\star$), the beam is vertical at its midpoint when the indentor force and displacement y_0 vanish, i.e. when it reaches the antisymmetric mode 2 solution from which it subsequently snaps. For $d > d_\star$, the beam reaches this point earlier in the deformation, and thereafter takes a multi-valued 'S' shape in the antisymmetric state. As the experimental indentor cannot maintain contact with a vertically sloping beam (or beyond), such deformations are experimentally inaccessible; $d_\star$ forms an upper limit on the end-shortenings that can be interrogated experimentally. To find the critical height corresponding to $d_\star$, we need only focus on the antisymmetric mode 2 solution, and find the value of d at which the slope $\theta(0)$ passes $\pi/2$. Such a plot is given in Fig. A.2; we find the critical value $d_\star \approx 0.34$.

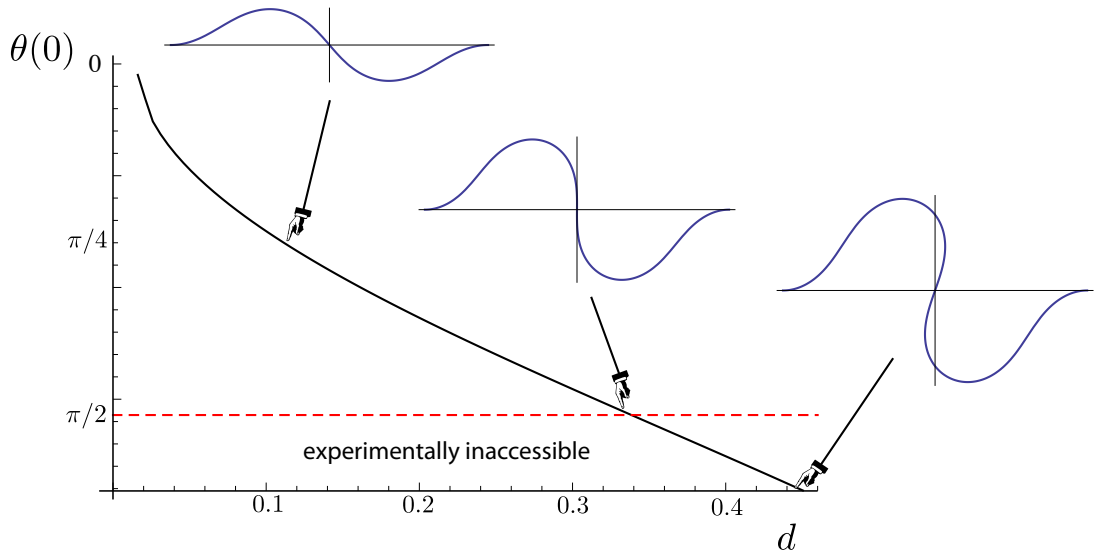

Figure A.2: The slope at the midpoint in the antisymmetric mode 2 solution plotted against the end-shortening d. Beyond $d_\star \approx 0.34$, the beam shape becomes multi-valued and so is inaccessible experimentally.

A.4.3 Dynamics

To explore dynamics, we set $f = 0$ and perform a linear stability analysis in the same manner as in Section A.3, but here we must add a perturbation to all variables; that is we expand $x = x_\nu + \epsilon x_p e^\sigma t$, $y = y_\nu + \epsilon y_p e^\sigma t$, etc. The system at $O(\epsilon)$ is

$$\begin{aligned}
x_p' &= \alpha_p \cos\theta_\alpha - \alpha_\nu \theta_p \sin\theta_\alpha \\
y_p' &= \alpha_p \sin\theta_\alpha + \alpha_\nu \theta_p \cos\theta_\alpha \\
n_{x_p}' &= \sigma^2 x_p \\
n_{y_p}' &= \sigma^2 y_p \\
\theta_p' &= m_p \\
m_p' &= \alpha_p n_{x_\nu} \sin\theta_\alpha + \alpha_\nu n_{x_p} \sin\theta_\nu + \alpha_\nu n_{x_\nu} \theta_p \cos\theta_\nu \\
&\quad - \alpha_p n_{y_\nu} \cos\theta_\nu - \alpha_\nu n_{y_p} \cos\theta_\nu + \alpha_\nu n_{y_\nu} \theta_p \sin\theta_\nu
\end{aligned} \tag{A.68}$$

with

$$\alpha_p = \mathcal{S}\left(n_{x_p} \cos\theta_\nu - n_{x_\nu} \theta_p \sin\theta_\nu + n_{y_p} \sin\theta_\nu + n_{y_\nu} \theta_p \cos\theta_\nu\right). \tag{A.69}$$

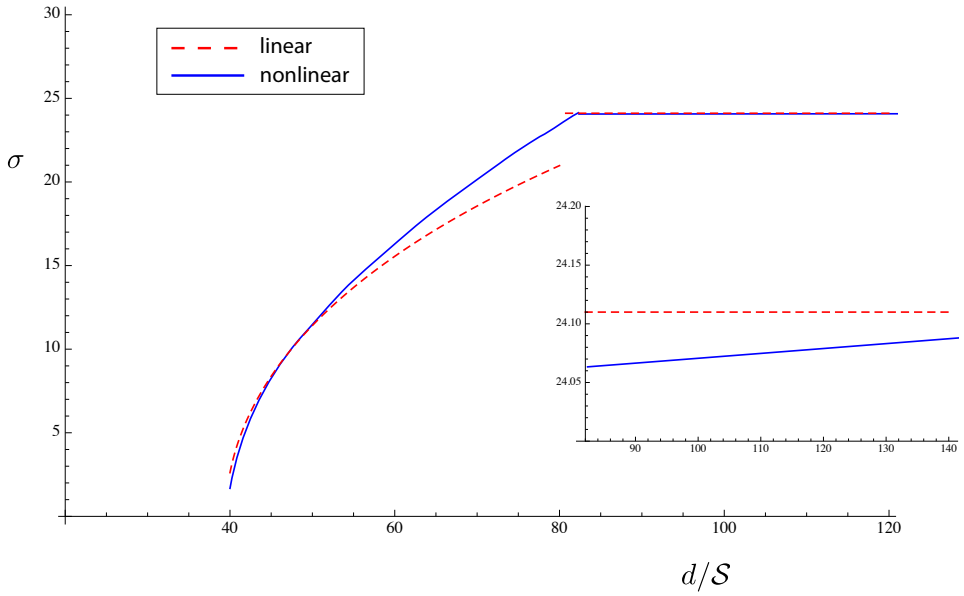

Figure A.3: Growth rate of snap-through instability for FvK (linear) and Kirchhoff (nonlinear) models.

The boundary conditions at $O(\epsilon)$ are

$$x_p = y_p = \theta_p = 0 \quad \text{at } S = \pm 1/2. \tag{A.70}$$

To solve (A.68) - (A.70) for a given equilibrium solution $\{x_\nu, y_\nu, n_{x_\nu}, \dots\}$, we implemented a determinant method, integrating three copies of the system from $S = -1/2$ with linearly independent initial conditions. We then formulate the boundary conditions at $S = 1/2$ as a determinant condition $\det M = 0$, where $M = M(\sigma^2)$ is a matrix consisting of the boundary conditions (A.70) for each of the three copies. If the system admits any solution with $\sigma^2 > 0$, the equilibrium solution is unstable and σ defines the growth rate of the instability; if the determinant condition can only be satisfied for $\sigma^2 < 0$, the equilibrium solution is stable and the values $\omega = \sqrt{-\sigma^2}$ define the ringing frequencies.

In Fig. A.3, we plot the growth rate σ against $d/\mathcal{S}$ for both Kirchhoff and FvK models. In the regime $d/\mathcal{S} < 80.76$, the curved dashed line follows the approximation (A.52). For $d/\mathcal{S} > 80.76$ (inset), the Kirchhoff theory predicts a small increase in σ with $d/\mathcal{S}$, but is well approximated by the FvK result $\sigma \approx 24.11$.

Fig. A.4 gives a comparison of ringing frequencies for the two models. The horizontal dashed

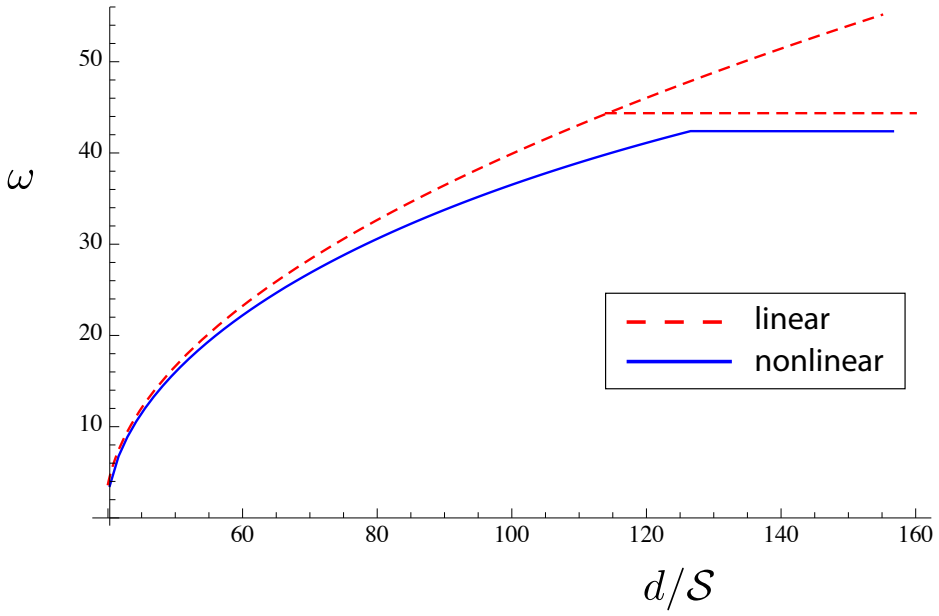

Figure A.4: Comparison of ringing frequency for FvK (linear) versus Kirchhoff (nonlinear).

line corresponds to the computed value $\omega \approx 44.36$, while the curved dashed line is given by formula (A.58).

A.5 Vibrations of a spherical shell

In this section we outline the calculation of the vibration frequency of a spherical cap. We consider a spherical cap with base diameter L, radius of curvature R, and thickness h. (Note that the base diameter corresponds most closely to the width of the two-dimensional arches that we considered previously and so we use the same notation.) The normal displacement of the shell, denoted w, and the Airy stress function, denoted ϕ, can be described by the Donnell-Mushtari-Vlasov equations, which read [2]

$$\begin{aligned} B\Delta^2 w + \frac{1}{R}\Delta\phi + \rho_s h\frac{\partial^2 w}{\partial t^2} &= 0 \\ \Delta^2\phi - \frac{Eh}{R}\Delta w &= 0. \end{aligned} \tag{A.71}$$

Here ρ_s is the density and $B = Eh^3/12(1-\nu^2)$ is the bending stiffness (with Poission ratio ν and Young's modulus E). The first of these equations expresses vertical force balance; the second expresses the compatibility of strains and allows us to deduce

$$\Delta\phi = \frac{Eh}{R}w. \tag{A.72}$$

Inserting (A.72) into the first equation of (A.71), we obtain

$$B\Delta^2 w + \frac{Eh}{R^2}w + \rho_s h\frac{\partial^2 w}{\partial t^2} = 0. \tag{A.73}$$

To find the vibration frequency of the popper, we perform a linear stability analysis assuming the shell remains radially symmetric. Writing

$$w = w(r)e^{i\omega t},$$

where r is the radial coordinate, we have

$$B\Delta^2 w + \left(\frac{Eh}{R^2} - \rho_s h\omega^2\right) w = 0 \tag{A.74}$$

where the symmetric Laplacian operator reads

$$\Delta w = w''(r) + \frac{1}{r}w'(r).$$

The popper is clear of the table when in the ringing state, thus we impose boundary conditions at the edge of the shell ($r = L/2$) corresponding to a free edge:

$$\Delta w = \frac{d}{dr}\Delta w = 0 \quad \text{at } r = L/2. \tag{A.75}$$

Along with this, we have the following two conditions at the centre of the shell

$$w'(0) = w'''(0) = 0, \tag{A.76}$$

which ensure that no force is applied at the centre for the radially symmetric deformation.

To non-dimensionalize the problem, we scale lengths by the bending length

$$l_b = \left(\frac{BR^2}{Eh}\right)^{1/4}.$$

That is, we write $\tilde{w} = w/l_b$, $\tilde{r} = r/l_b$. This natural length scale introduces the dimensionless frequency

$$\Omega = \left(\frac{\rho_s R^2}{E}\right)^{1/2} \omega = \frac{R}{c}\omega$$

where, as in the main paper, c is the speed of sound in the material. Inserting these scalings in (A.74) and dropping tildes henceforth, the dimensionless problem is

$$\begin{aligned} &\Delta^2 w + (1-\Omega^2)w = 0 \\ &w'(0) = w'''(0) = 0 \\ &\Delta w(a) = \frac{d}{dr}\Delta w(a) = 0, \end{aligned} \tag{A.77}$$

where $a = L/(2l_b)$. We note that this eigenproblem is mathematically identical to the problem of the ringing of a circular disc with free edges, albeit with a shifted frequency. This is an example of the more general result of [3] that such shell problems always reduce to the corresponding plate problem with the same boundary conditions and a modified frequency.

The general solution to (A.77), subject to the boundary conditions at $r = 0$ (and a finite solution constraint at $r = 0$) is

$$w(r) = AJ_0\left(r\left(\Omega^2-1\right)^{1/4}\right) + BI_0\left(r\left(\Omega^2-1\right)^{1/4}\right),$$

where J_0 and I_0 are Bessel functions of zeroth order, and A, B, are constants to be determined.

The linear stability analysis consists in finding the values of Ω for which w has a non-trivial solution satisfying the boundary conditions at $r = a$, (A.75). This leads to the determinant

condition $\det(M) = 0$ where

$$M(\Omega) = \begin{pmatrix} I_0\left(a\left(\Omega^2-1\right)^{1/4}\right) & -J_0\left(a\left(\Omega^2-1\right)^{1/4}\right) \\ I_1\left(a\left(\Omega^2-1\right)^{1/4}\right) & J_1\left(a\left(\Omega^2-1\right)^{1/4}\right) \end{pmatrix}. \tag{A.78}$$

We find numerically that the smallest solution of this is given by

$$a\left(\Omega^2-1\right)^{1/4} \approx 3.196 =: \lambda$$

Inserting this into the scalings, and recalling the characteristic timescale $t_* = 2\sqrt{3}\frac{L^2}{ch}$ defined in section A.1 and used in the main paper, we obtain the following expression for the dimensional ringing frequency:

$$\omega^2 = \frac{c^2}{R^2} + 16\frac{\lambda^4}{1-\nu^2}\frac{1}{t_*^2}. \tag{A.79}$$

From this, the ringing period $t_r := 2\pi/\omega$ can be expressed as

$$t_r = \frac{\pi\sqrt{1-\nu^2}}{2\lambda^2} t_* (1+\epsilon)^{-1/2}, \tag{A.80}$$

where we anticipate that

$$\epsilon := \frac{3}{4}\frac{1-\nu^2}{\lambda^4}\frac{L_{\text{base}}^4}{R^2h^2} \ll 1.$$

Indeed, for the typical popper experiments presented here, $L = R$, $R/h = 5$ and $\nu \approx 0.5$, which gives $\epsilon = 0.134$, while for the jumping disk $\epsilon = 0.003$. If we neglect the ϵ term, we obtain the universal shell relation

$$t_r \approx \frac{\pi\sqrt{1-\nu^2}}{2\lambda^2} t_* \approx 0.133 t_*.$$

References

[1] B. Audoly and Y. Pomeau. *Elasticity and Geometry.* Oxford University Press, 2010.

[2] W. Soedel. *Vibrations of Shells and Plates.* Marcel Dekker, 2004.

[3] W. Soedel. A natural frequency analogy between spherically curved panels and flat plates. *J. Sound Vib.*, 29:457–461, 1973.